# Power Spectrum Analysis of Modified HIJET Events

**Thomas A. Trainor**

*Nuclear Physics Laboratory GL-10*
*University of Washington*
*Seattle, WA 98195*

February 27, 1994

**Abstract**

I review here progress on analysis of event generator multiplicity distributions with differential autocorrelations and associated power spectra. The analysis is applied to twenty generator events, of which ten are normal HIJET events and ten are 'special' events which have had added one or two additional energy concentrations (van Hove 'plasma bubbles') at specific points in rapidity. There is a strong 2-D relationship between certain features of the power spectra and rapidity moments of the added energy distributions. These features (total power and phase) can be used to form a 'pattern space' in which there is excellent separation between normal and special events.

## 1 Introduction

In previous work[][] I have presented a type of autocorrelation and power spectrum analysis of charged particle multiplicity distributions which is constructed by analogy with electrical signal analysis. The problems are formally identical, with a distribution of hits on a continuous index manifold (electrons on time or particles on pseudorapidity) from which a signal (event characterization) is to be inferred. The Poisson noise in the multiplicity distribution is identical to shot noise in an electrical current.

In the first one-dimensional applications of this technique[] I generated a series of uniform random hit distributions (trials) on 100 bins, with mean occupancy of 10 hits per bin. I then introduced by hand additional gaussian features having various positions, areas and widths. I found that certain quantities derived from the power spectra could form the coordinates of a 'pattern space,' and that the location of a trial in this pattern space enabled prediction of the qualities of the features added to that trial, or whether any feature had been added, within some confidence limit.

I then extended this work to the two-dimensional case[]. The 1-D case seems more applicable to anomalous or nonlinear QCD stopping and plasma phenomena (where phi dependence may be minimal), whereas the 2-D case seems more amenable to jet/minijet analysis (especially when an EM calorimeter or particle tracking is available).

In the present work I extend the 1-D analysis to event generator outputs. Twenty events are considered, of which ten are normal HIJET events, and ten have had some fraction of the total stopped energy placed at specific points in rapidity to emulate van Hove plasma bubbles. The placements amount to a total of 1-5 TeV at one or two rapidity points.

I include plots from the various stages of the power spectrum analysis, and finally show the twenty events on a pattern space derived from the power spectra. The results indicate that such analysis provides important, model-independent information on the nature of the QCD energy transport process in nucleus-nucleus collisions and may serve as a powerful trigger algorithm.

## 2 Event Generator Output

The generator events used here were constructed to examine the ability of various trigger algorithms to detect 'anomalous' particle distributions. By this means algorithms can be calibrated as to the nature and sensitivities of the signals that may be produced by each algorithm in comparison to the anomalies which serve as input. In this study the input is twenty HIJET events produced by Ron Longacre of BNL[], of which ten have been modified by him to simulate anomalous QCD stopping behavior or QGP phase transitions. In this section I first discuss the 'reasonableness' of these anomalous events. Then I describe the events themselves and a method of parameterizing them for the purpose of trigger algorithm calibration.

The total collision system energy at RHIC for Au-Au at 100 GeV/u is about 40 TeV. Using generator event twelve (Fig. 3) as a typical normal event I estimate very crudely that the total energy in these 'detectable' particles for a normal event is 6,000 particles $\cdot$ 1 GeV/particle = 6 TeV. If I do the same analysis on event 9 in the same figure I find that the normal background contains about 4,000 particles = 4 TeV, and the obvious 'bubble' contribution contains about 2,400 particles = 2.4 TeV. This estimate for the bubble energy agrees pretty well with the actual inserted energy (2.6 TeV, see Table 1). So the by-hand placed energies in the anomalous events correspond to a range of 0.2 to 1.0 times the normal detected energy, and the *total* detected energy of one of these plasma events is not significantly different from that for a normal event in the way that this simulation was performed.

Whether these *ad hoc* energy placements represent a reasonable signal or nonlinear fluctuation in the stopping process, or the degree to which the total stopped energy should also fluctuate, is a matter of taste at this point. However, the analysis results are useful at any rate because one can relate these results by scaling to later predictions from more sophisticated arguments.

First I give the parameters of the bubble energies (GeV) and placements in Table 1. Then I show in Figs. 1 – 5 HIJET outputs for the twenty generator events. In these figures the variations in multiplicity over the full range of $\eta$ associated with the bubble placements are very apparent to the eye.

In order to form a basis for comparison with the power spectrum analysis below I have defined moments of these energy distributions.

$$E_{tot} = \sum_i E_i \tag{1}$$

and

$$Q_2 = 0.8(1 - 0.4 \sum_i y_i^2 E_i / E_{tot}), \tag{2}$$

where for a bubble event $i = 1$ or 1,2 depending on the number of bubbles, $E_i$ is the energy of the $i^{th}$ bubble, and $y_i$ is the rapidity of the $i^{th}$ bubble. The ten bubble events are plotted on the $(E_{tot}, Q_2)$ space in Fig. 6. The constants in the definition of $Q_2$ were chosen to facilitate comparison of the event distribution on $(E_{tot}, Q_2)$ with the distribution on the power/phase space shown in Fig. 27. They are not intended to have physical significance.

| event number | bubble number | minus rapidity | plus rapidity | minus energy | plus energy |
|---|---|---|---|---|---|
| 1 | 1 | -0.1 | | 1843 | |
| 2 | 0 | | | | |
| 3 | 2 | -2.4 | 2.2 | 500 | 480 |
| 4 | 1 | | 1.2 | | 1117 |
| 5 | 0 | | | | |
| 6 | 1 | -1.3 | | 1248 | |
| 7 | 0 | | | | |
| 8 | 0 | | | | |
| 9 | 1 | | 0.0 | | 2649 |
| 10 | 2 | -2.0 | 2.1 | 926 | 938 |
| 11 | 2 | -2.2 | 2.2 | 1203 | 1145 |
| 12 | 0 | | | | |
| 13 | 0 | | | | |
| 14 | 0 | | | | |
| 15 | 0 | | | | |
| 16 | 0 | | | | |
| 17 | 2 | -1.8 | 1.7 | 1896 | 1843 |
| 18 | 2 | -1.5 | 1.4 | 2500 | 2314 |
| 19 | 0 | | | | |
| 20 | 2 | -1.3 | 1.1 | 1457 | 1452 |

Table 1: Plasma bubble parameters

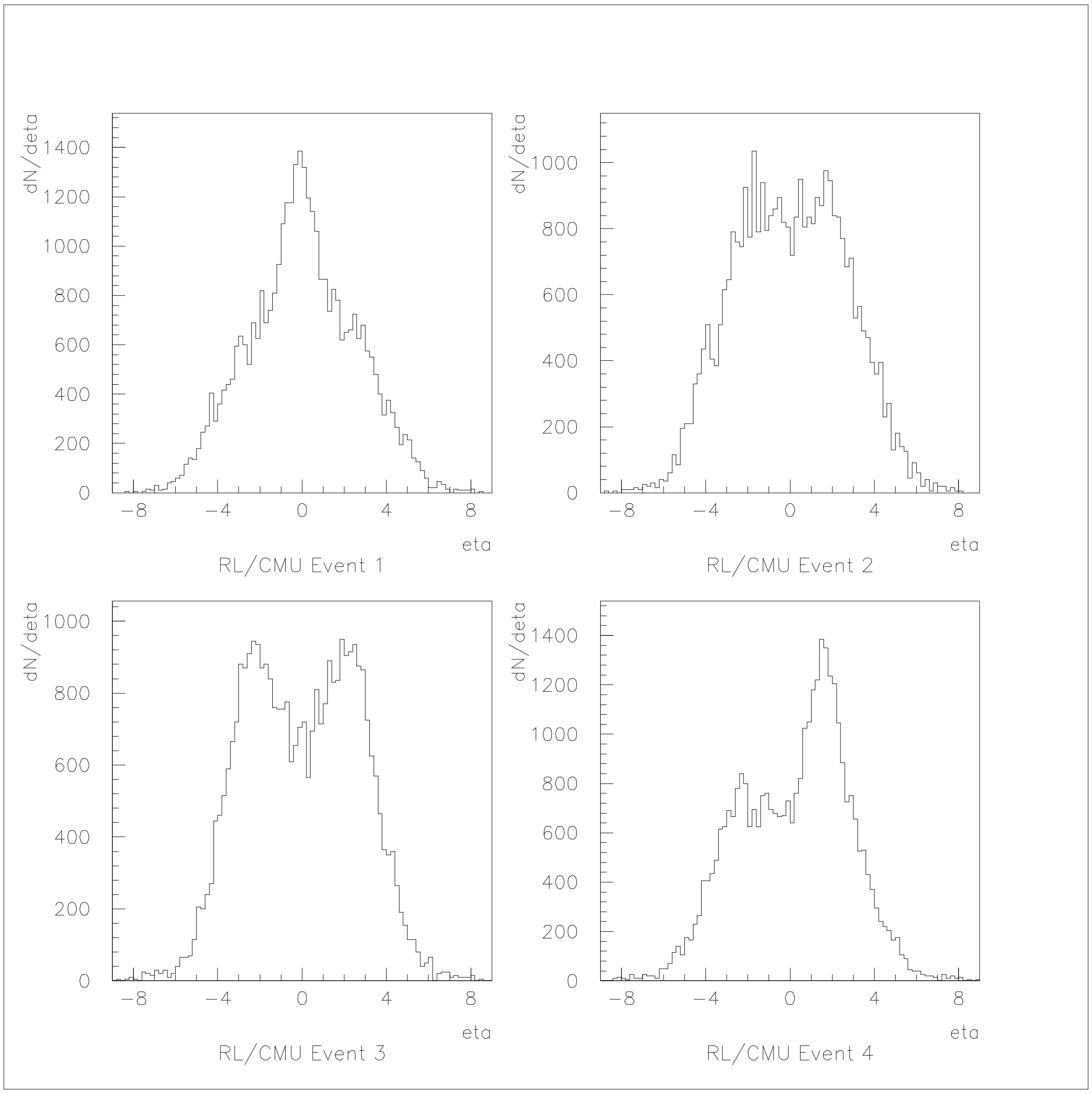
dN/deta
1400
1200
1000
800
600
400
200
0
−8
−4
0
4
8
eta
RL/CMU Event 1
dN/deta
1000
800
600
400
200
0
−8
−4
0
4
8
eta
RL/CMU Event 2
dN/deta
1000
800
600
400
200
0
−8
−4
0
4
8
eta
RL/CMU Event 3
dN/deta
1400
1200
1000
800
600
400
200
0
−8
−4
0
4
8
eta
RL/CMU Event 4

Figure 1:

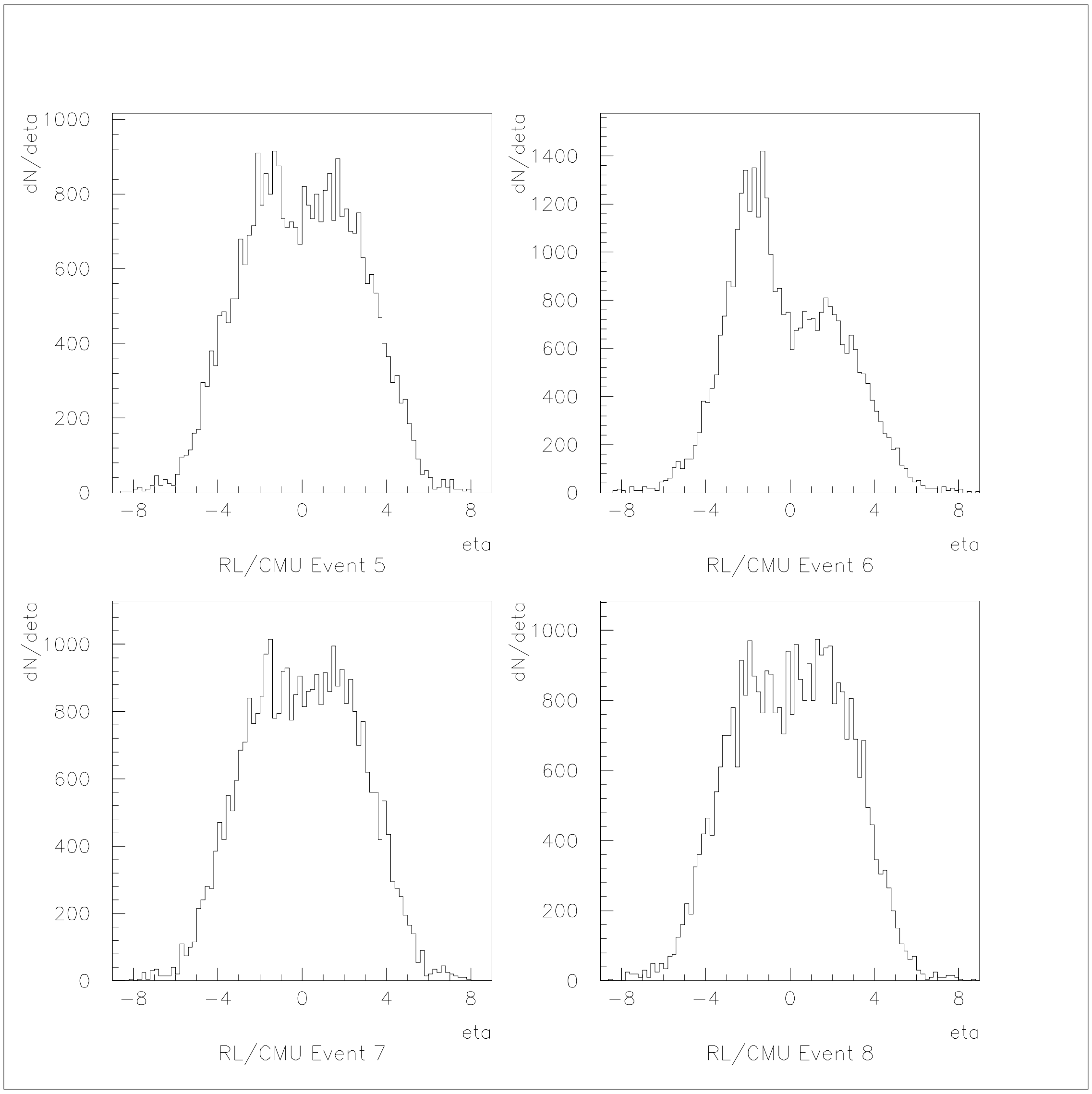
dN/deta
1000
800
600
400
200
0
−8
−4
0
4
8
eta
RL/CMU Event 5
dN/deta
1400
1200
1000
800
600
400
200
0
eta
RL/CMU Event 6
RL/CMU Event 7
RL/CMU Event 8

Figure 2:

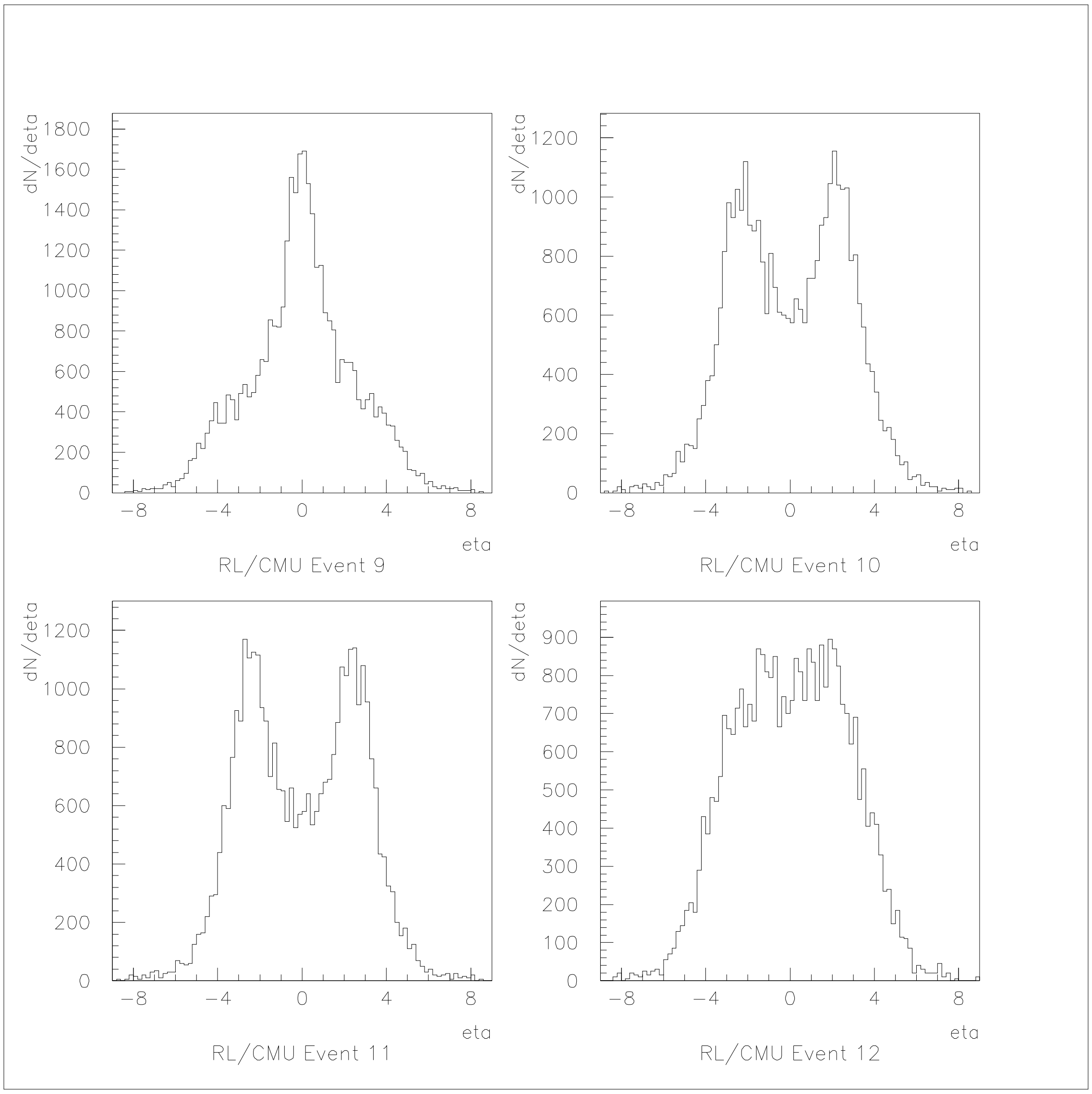
dN/deta
eta
RL/CMU Event 9
RL/CMU Event 10
RL/CMU Event 11
RL/CMU Event 12

Figure 3:

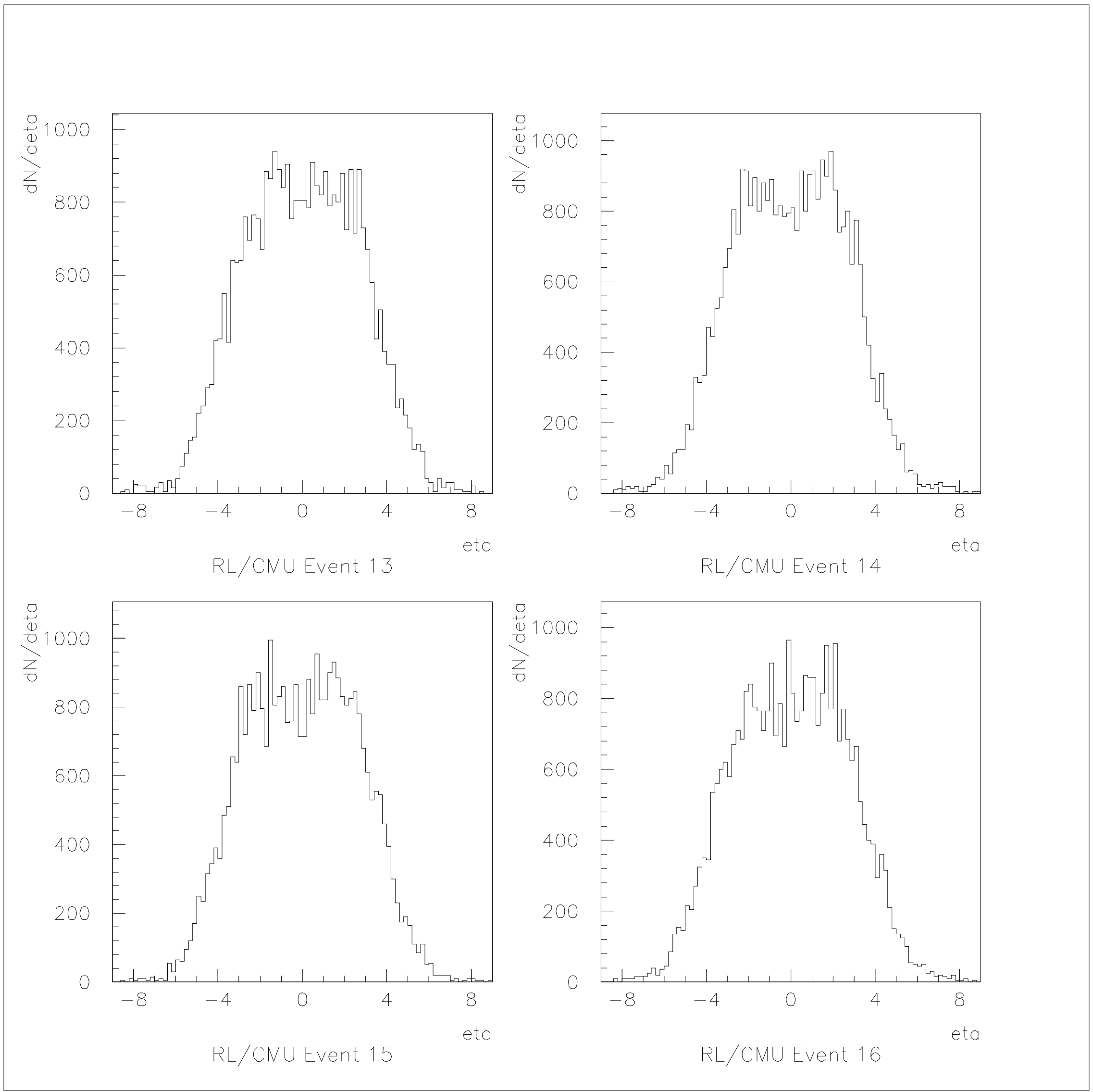
dN/deta
eta
RL/CMU Event 13
RL/CMU Event 14
RL/CMU Event 15
RL/CMU Event 16

Figure 4:

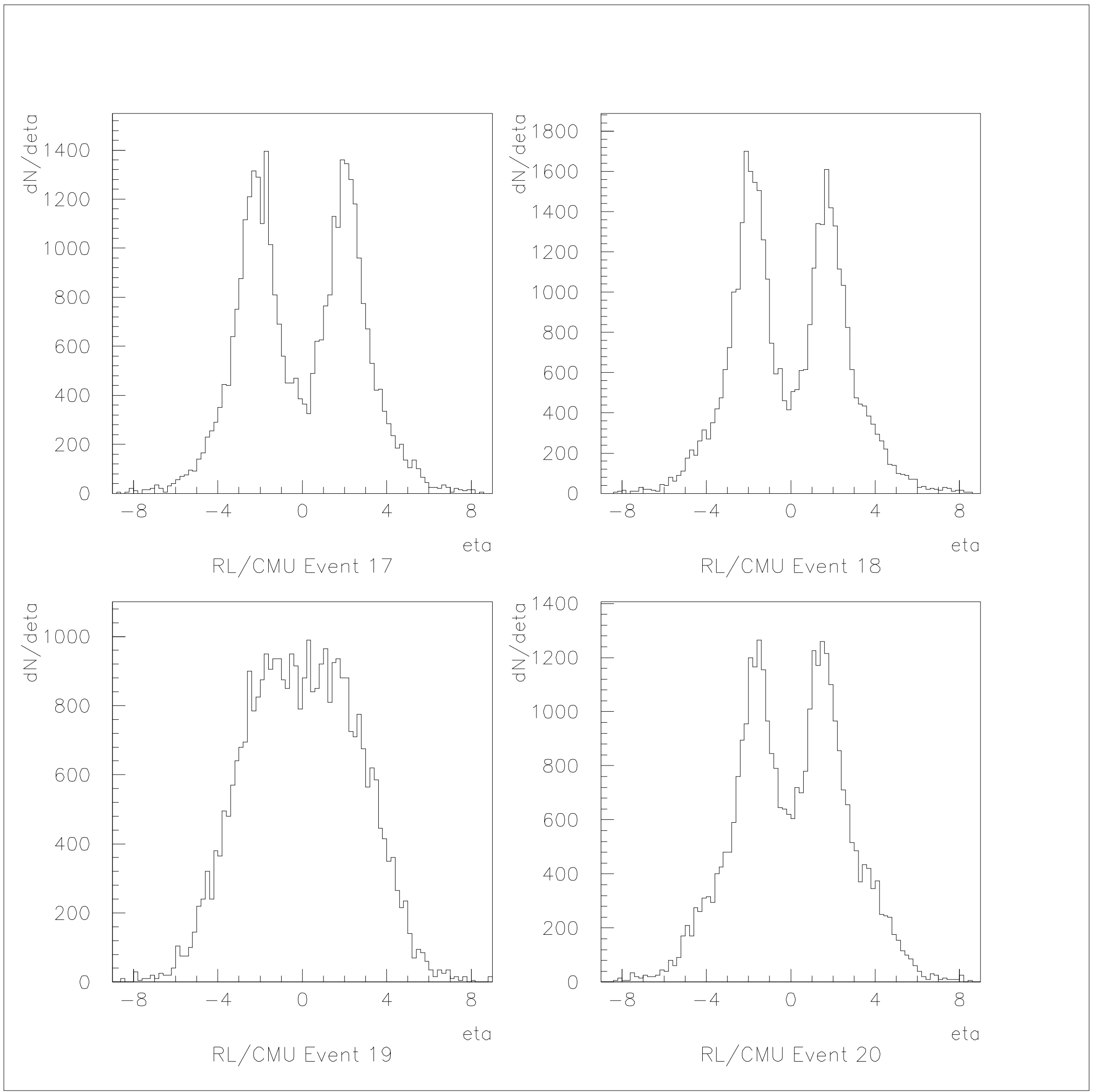
dN/deta
1400
1200
1000
800
600
400
200
0
−8
−4
0
4
8
eta
RL/CMU Event 17
dN/deta
1800
1600
1400
1200
1000
800
600
400
200
0
eta
RL/CMU Event 18
dN/deta
1000
800
600
400
200
0
eta
RL/CMU Event 19
dN/deta
1400
1200
1000
800
600
400
200
0
eta
RL/CMU Event 20

Figure 5:

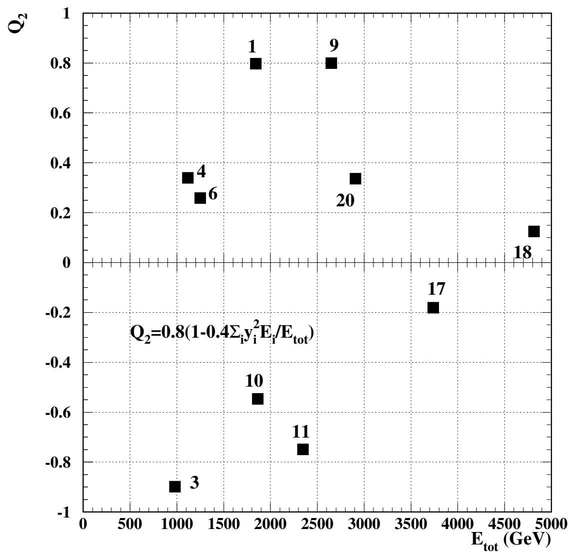


Figure 6: Plasma bubble moments

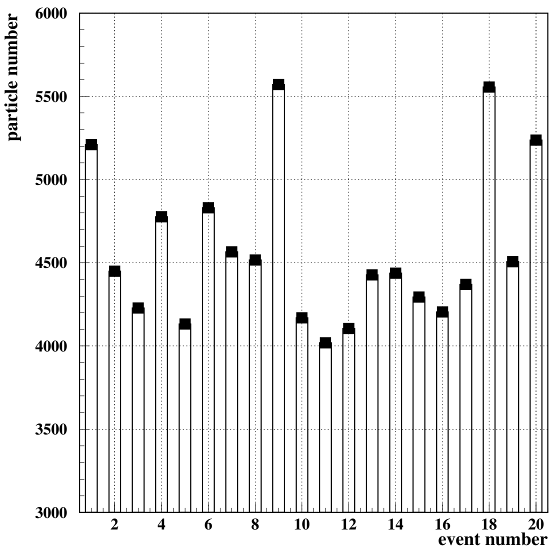


Figure 7: Event particle counts

## 3 Detected Multiplicities

Here I show combined GEANT outputs for hits registered in the trigger detectors CTB and MWC. These data were produced by Zoran Milosevich of CMU[] from the generator data presented above. For figures 8 through 10 I have binned the data into 5 bins per unit $\eta$ to match the binning of $\eta$ in the generator outputs.

If the trigger detectors were perfect within their geometrical acceptances and with zero mass I would expect a reproduction of the generator charged particle output over the interval $\eta$ = [-2,2] in the GEANT plots. I observe that the total number of trigger detector hits in each of the GEANT files is 4000-5500, whereas the total output from the normal generator events within the same geometrical acceptance is about 3,000 ($750 \cdot 4$). I include a plot of the GEANT particle counts in the various events in Fig. 7.

A close look at the GEANT output for the normal events indicates that there is a consistent excess of hits in the MWC as compared to the CTB, by as much as 50% (e.g., event 5, Fig. 8). And the $\eta$ dependence of particle yield into the two detector acceptances does not match at the mutual boundaries. An investigation of this behavior and determination of detector efficiency on ($P_t$,$y$) for the trigger detectors are in progress. These anomalies should of course be resolved in the near future. I present here work in progress. One should also note in Figs. 13 – 17 the effect of the gap between the CTB and MWC acceptances, especially in the autocorrelations at bins 28 and 72.

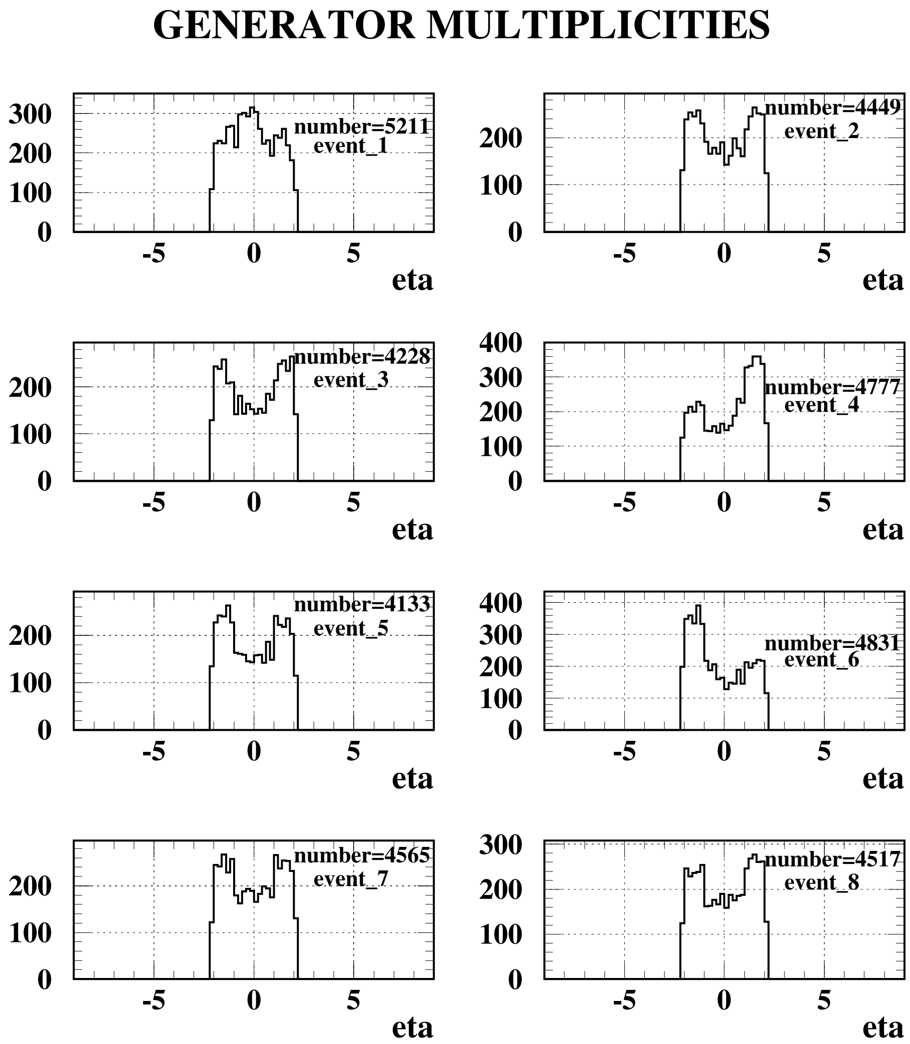
GENERATOR MULTIPLICITIES
number=5211
event_1
number=4449
event_2
number=4228
event_3
number=4777
event_4
number=4133
event_5
number=4831
event_6
number=4565
event_7
number=4517
event_8
eta

Figure 8:

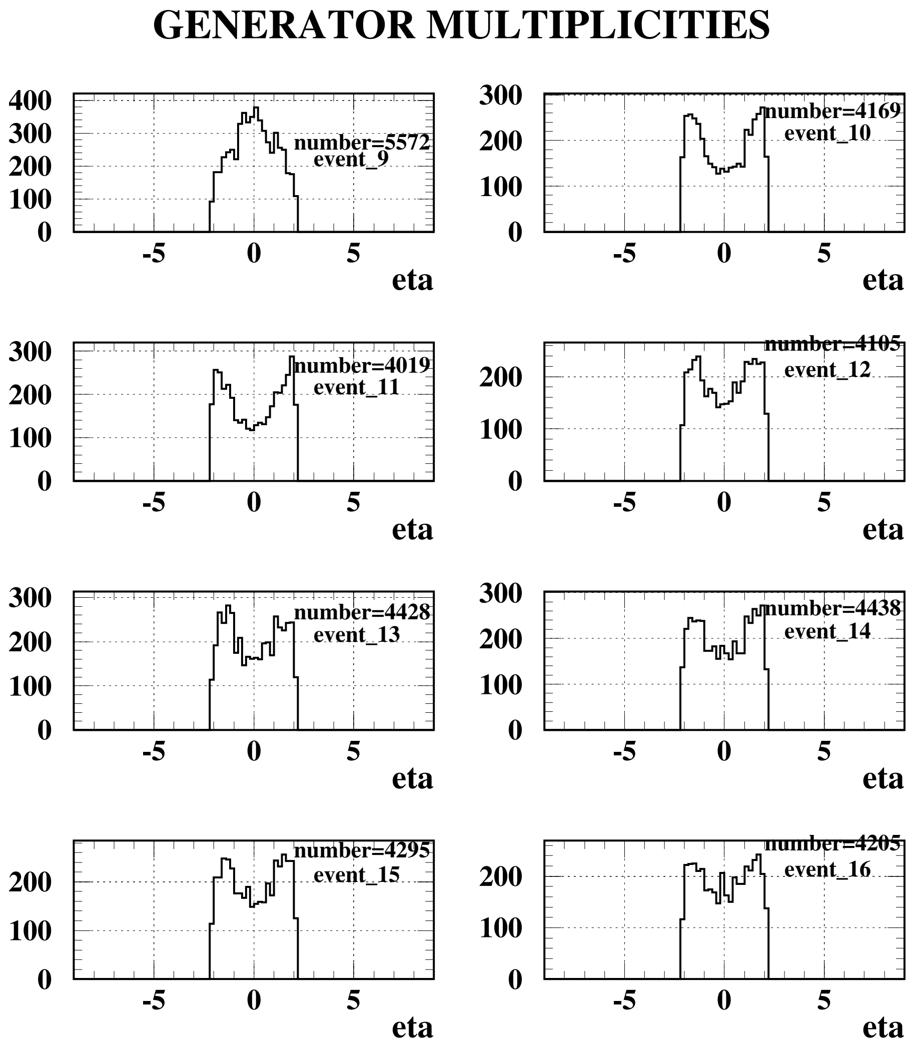
GENERATOR MULTIPLICITIES
number=5572
event_9
number=4169
event_10
number=4019
event_11
number=4105
event_12
number=4428
event_13
number=4438
event_14
number=4295
event_15
number=4205
event_16
eta

Figure 9:

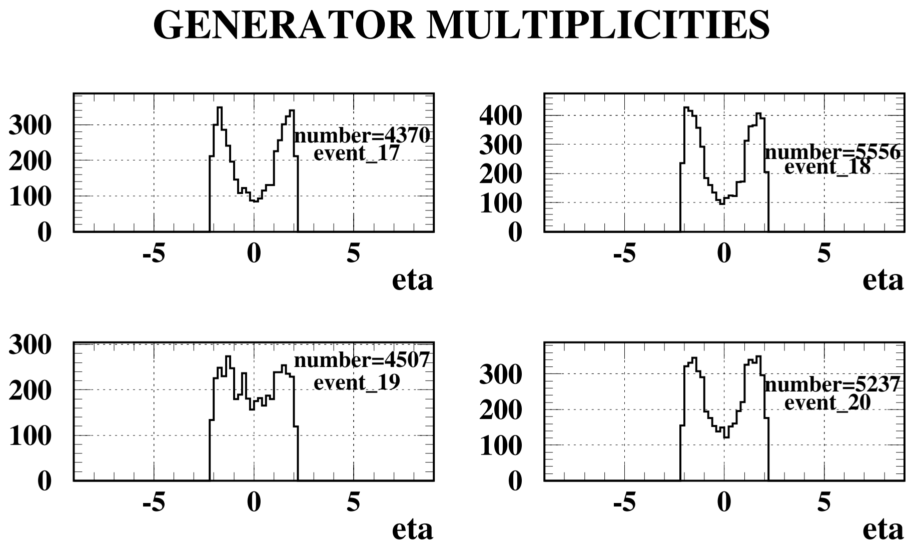
GENERATOR MULTIPLICITIES
number=4370
event_17
number=5556
event_18
number=4507
event_19
number=5237
event_20
eta
eta
eta
eta

Figure 10:

## 4 Autocorrelations

Here I define two types of autocorrelation for each event. These autocorrelations are discussed in my paper 'Autocorrelation Multiplicity Trigger - One-Dimensional Simulations.'[] These definitions include the standard or 'periodic' autocorrelation

$$A_m = \frac{1}{N}\sum_{i=1}^{N} f_i \cdot f_{i+m}^* \tag{3}$$

and the nonstandard or 'finite-domain' autocorrelation which I developed for this trigger application

$$B_m = \frac{1}{N-m}\sum_{i=1}^{N-m} f_i \cdot f_{i+m}^* . \tag{4}$$

Of the two it can be shown that the periodic autocorrelation is the even part (symmetric about the center of the domain) of the finite-domain (FD) autocorrelation, and that the latter therefore contains more information about the multiplicity distribution. Because it is not in general either symmetric or antisymmetric on the domain of definition the FD autocorrelation does not have a purely real (single component) Fourier transform (FT). In subsequent event analysis I will use only the FD autocorrelation, but I show both in this section for comparison.

This power spectrum event analysis is expected to deal with events having some distribution of *total* multiplicity which depends on lower-level trigger criteria. I would like to preserve the total multiplicity as an independent trigger criterion, and rely on the power spectrum analysis to discriminate only among *shapes* of distributions. Therefore I modify the autocorrelation definitions given in [] to normalized forms in terms of the mean yield per bin $< f >$ as

$$A'_m = \frac{1}{N}\sum_{i=1}^{N} f_i \cdot f_{i+m}^* / < f >^2 \tag{5}$$

and

$$B'_m = \frac{1}{N-m}\sum_{i=1}^{N-m} f_i \cdot f_{i+m}^* / < f >^2 . \tag{6}$$

What are actually plotted in the figures are *normalized differential* autocorrelations defined here as

$$a_m = 100(A'_m - 1 + M^{-1} - < f >^{-1}\, \delta_{m,0}) \qquad m \in \{0, N-1\}, \tag{7}$$

and

$$b_m = 100\frac{N-m}{N}(B'_m - 1 + M^{-1} - < f >^{-1}\, \delta_{m,0}) \qquad m \in \{0, N-1\} \tag{8}$$

for the periodic and FD differential autocorrelations respectively. As defined (including the factor 100) these quantities are the percent deviations from the autocorrelations of a Poisson distribution of total multiplicity $M$ on $N$ bins.

## 5 Null Hypothesis

The expressions in the previous section assume the simple case of a uniform Poisson background to form normalized differential autocorrelations. This Poisson background depends only on the total multiplicity $M$ falling on the domain of definition ($M =< f > \cdot N$). In the present case the 'normal' multiplicity distribution or *null hypothesis* resulting from HIJET and GEANT simulation of the trigger detectors has a noticable nonuniformity in the absolute autocorrelation on $\eta$. Therefore we must include a correction for this nonuniformity to define a true differential quantity. The goal is to produce an autocorrelation definition for which the corresponding power is minimal when a 'normal' event is detected. The method for doing this is actually quite systematic.

Taking the uniform Poisson background hypothesis one carries out a spectrum analysis of the residual differential autocorrelations for a set of normal events. These can be selected from the pattern space to be described below by some cut. These power spectra can be averaged to generate a null hypothesis correction for the differential autocorrelation. If this is done correctly the power for this population of events using the corrected differential autocorrelations will be minimized, and nonnormal events will have significant nonzero power and other features which can be used to discriminate. The corrected differential autocorrelations are then

$$a'_m = a_m + \sum_k as_k \cdot sin(2\pi \frac{k \cdot m}{100}) + ac_k \cdot cos(2\pi \frac{k \cdot m}{100}) \quad (9)$$

and

$$b'_m = b_m + \sum_k bs_k \cdot sin(2\pi \frac{k \cdot m}{100}) + bc_k \cdot cos(2\pi \frac{k \cdot m}{100}). \quad (10)$$

In practice this is very straightforward and systematic. Only a few terms are needed in the correction. As an example I show the correction that will be used in subsequent analysis sections which I determined from the power spectra as described above

$$b'_m = b_m + 7.5 \cdot sin(2\pi \frac{1 \cdot m}{100}) - 0.8 \cdot sin(2\pi \frac{2 \cdot m}{100}) - 1.0 \cdot sin(2\pi \frac{3 \cdot m}{100}) - 1.5 \cdot cos(2\pi \frac{1 \cdot m}{100}). \quad (11)$$

These coefficients were determined from the ensemble of normal HIJET events. This complete form of $b'_m$ is included from now on in the definition of the normalized differential autocorrelation as used below.

To illustrate this procedure I show in the following two figures the differential autocorrelations for the twenty HIJET events corrected only for a uniform Poisson component, with the null hypothesis correction given above (with sign reversed) superposed. In the remaining autocorrelation figures and subsequent analysis the full differential form with null hypothesis is used.

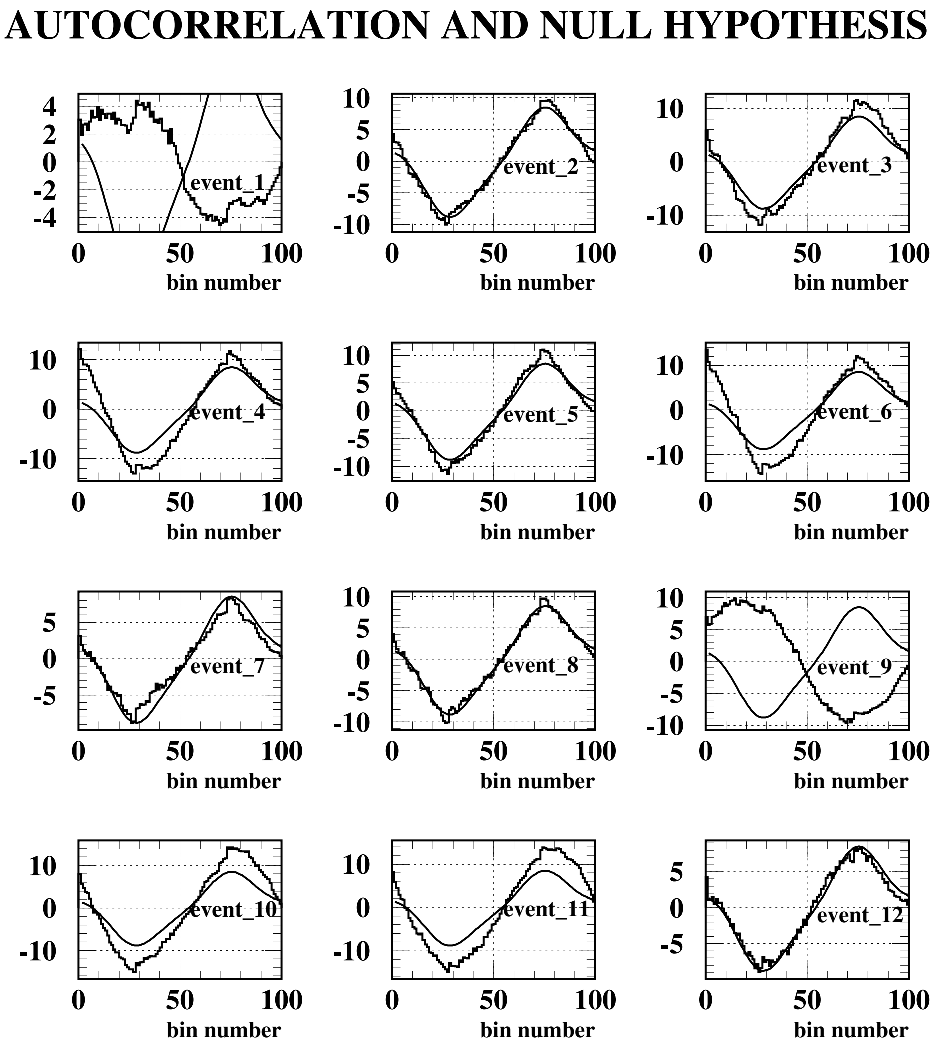
AUTOCORRELATION AND NULL HYPOTHESIS
event_1
event_2
event_3
event_4
event_5
event_6
event_7
event_8
event_9
event_10
event_11
event_12
bin number

Figure 11:

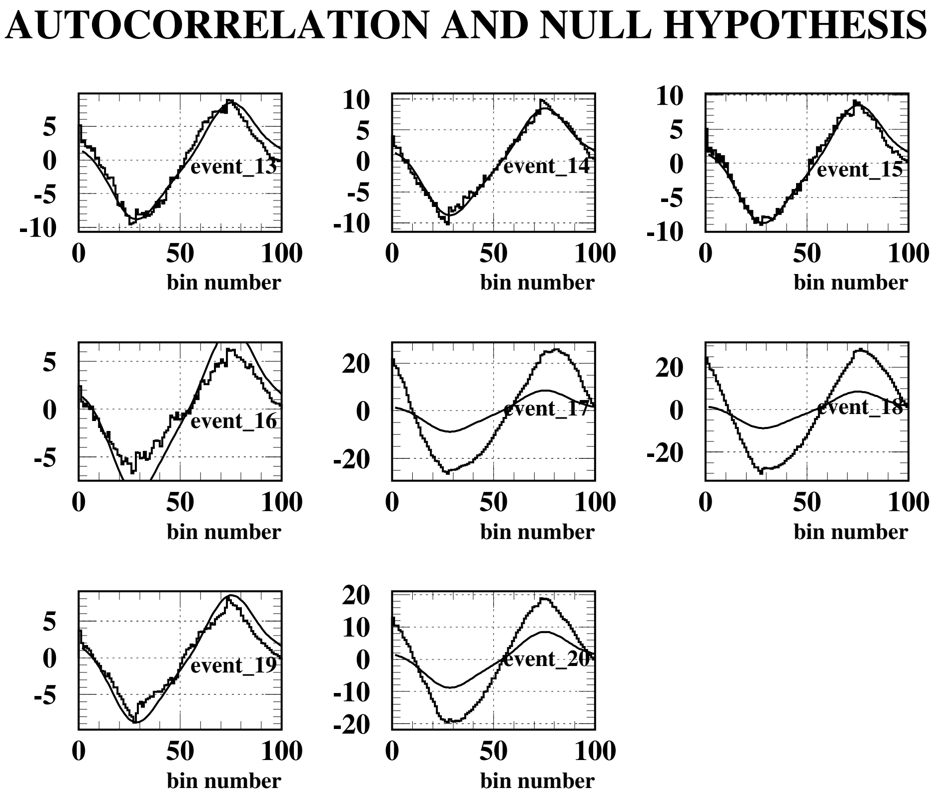
AUTOCORRELATION AND NULL HYPOTHESIS
event_13
event_14
event_15
event_16
event_17
event_18
event_19
event_20
bin number

Figure 12:

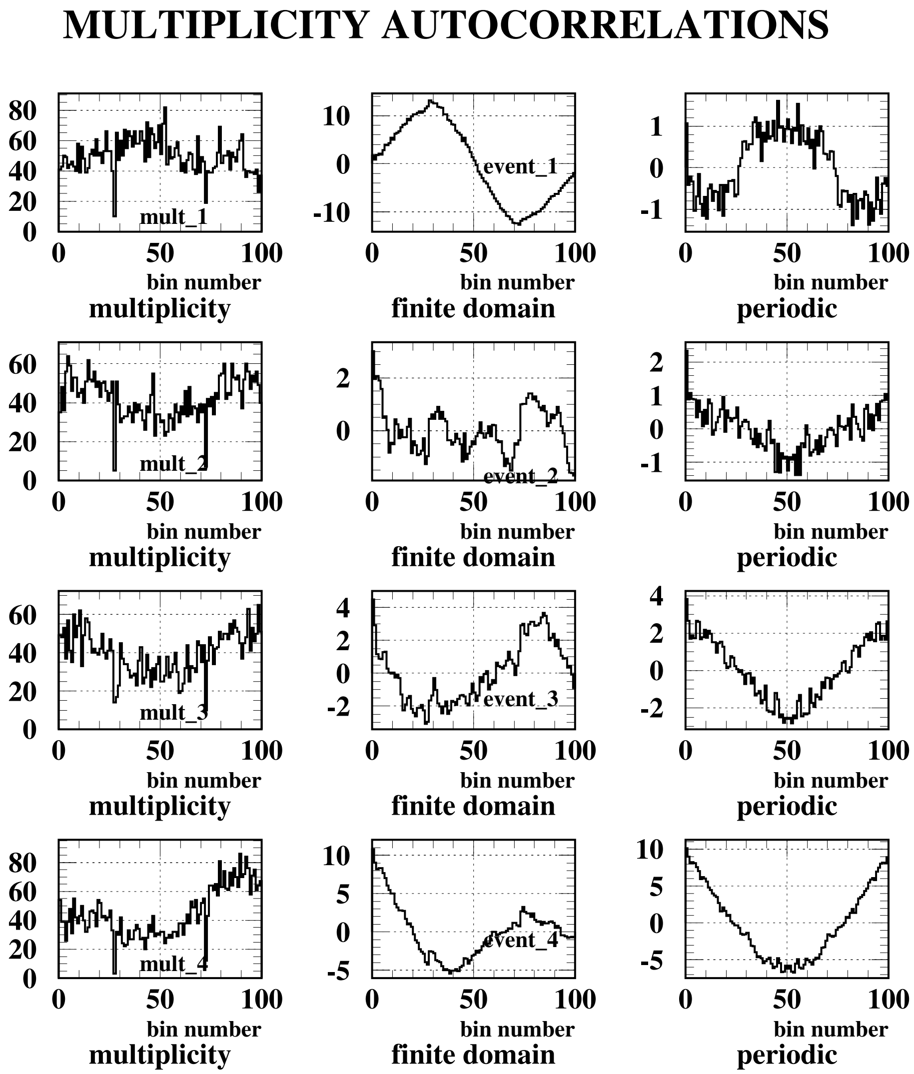
MULTIPLICITY AUTOCORRELATIONS
mult_1
event_1
mult_2
event_2
mult_3
event_3
mult_4
event_4
bin number
multiplicity
finite domain
periodic

Figure 13:

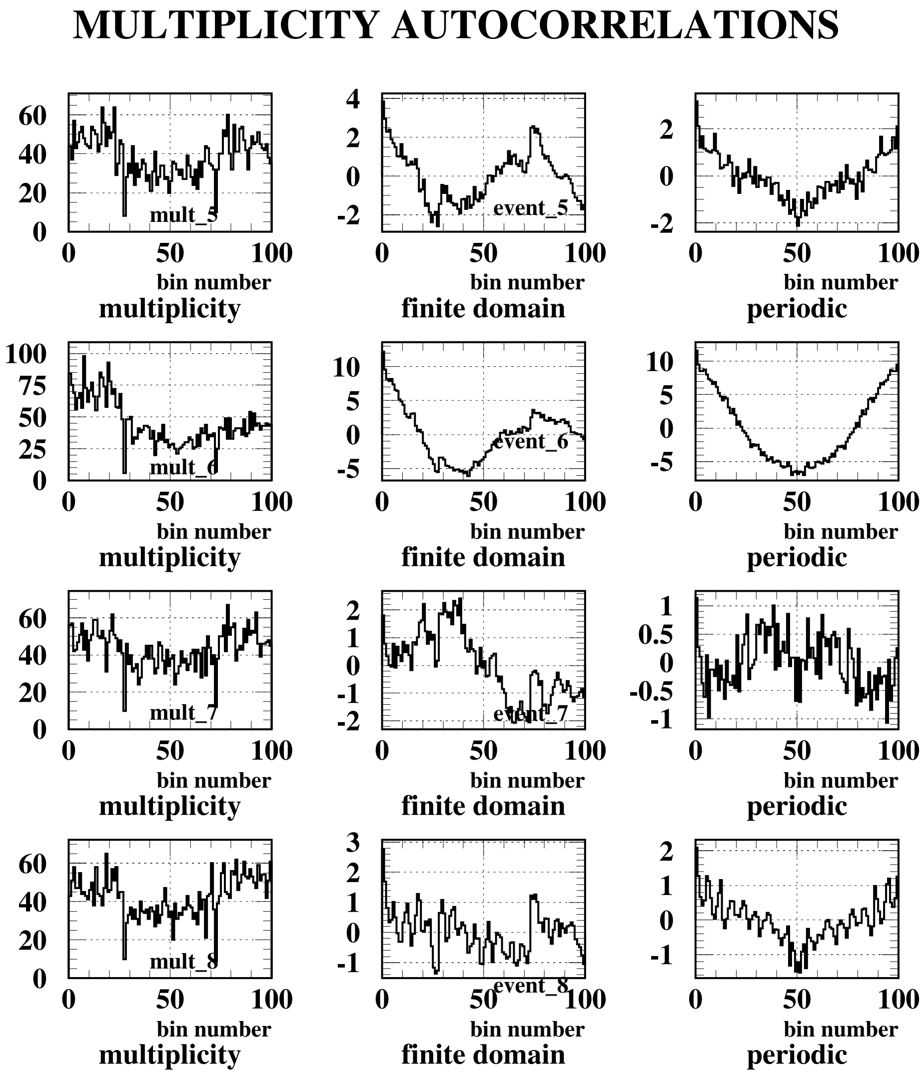
MULTIPLICITY AUTOCORRELATIONS
mult_5
event_5
bin number
multiplicity
finite domain
periodic
mult_6
event_6
mult_7
event_7
mult_8
event_8

Figure 14:

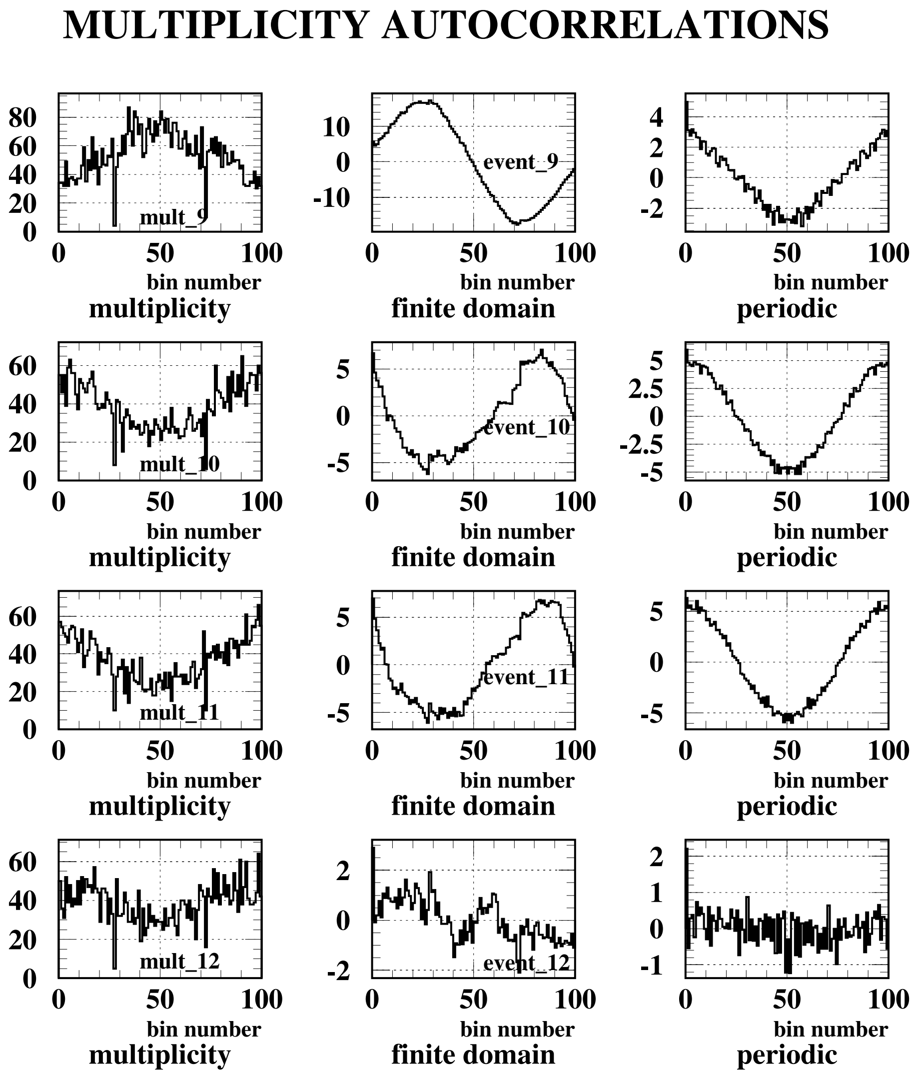
MULTIPLICITY AUTOCORRELATIONS
mult_9
event_9
mult_10
event_10
mult_11
event_11
mult_12
event_12
bin number
multiplicity
finite domain
periodic

Figure 15:

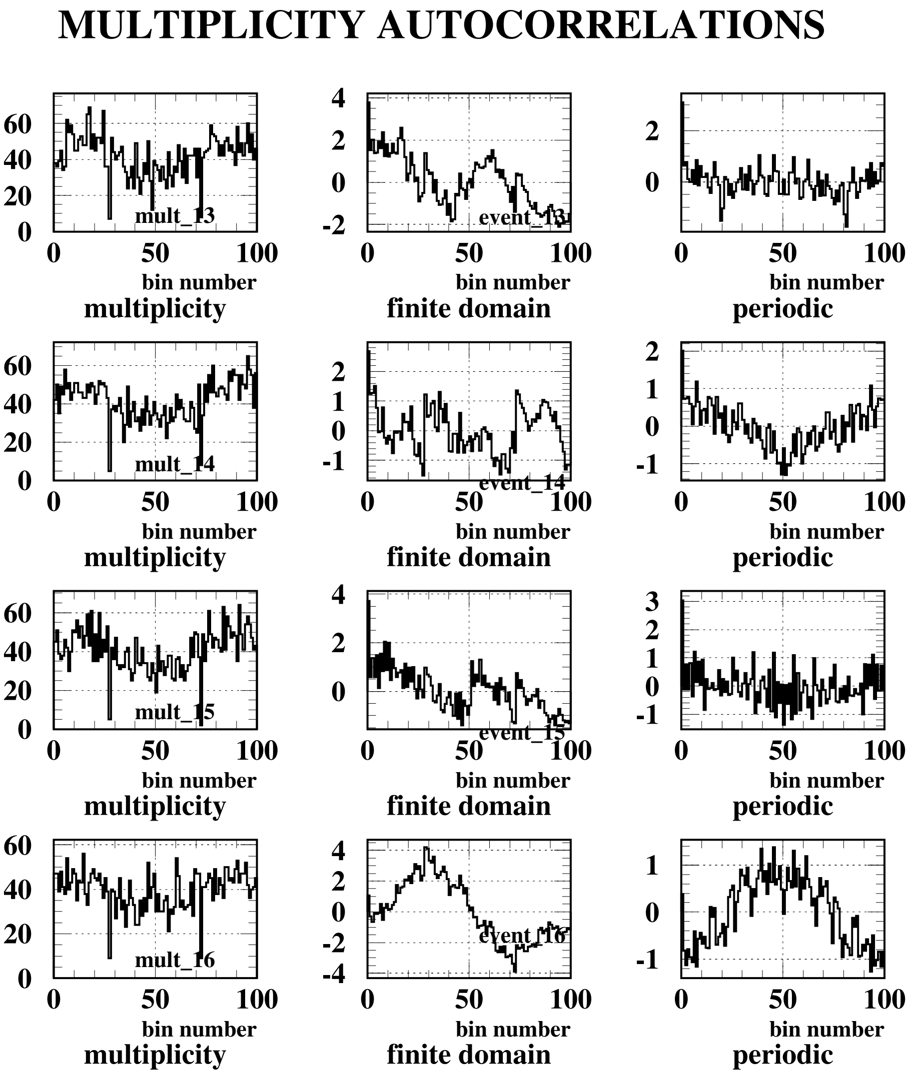
MULTIPLICITY AUTOCORRELATIONS
mult_13
event_13
mult_14
event_14
mult_15
event_15
mult_16
event_16
bin number
multiplicity
finite domain
periodic

Figure 16:

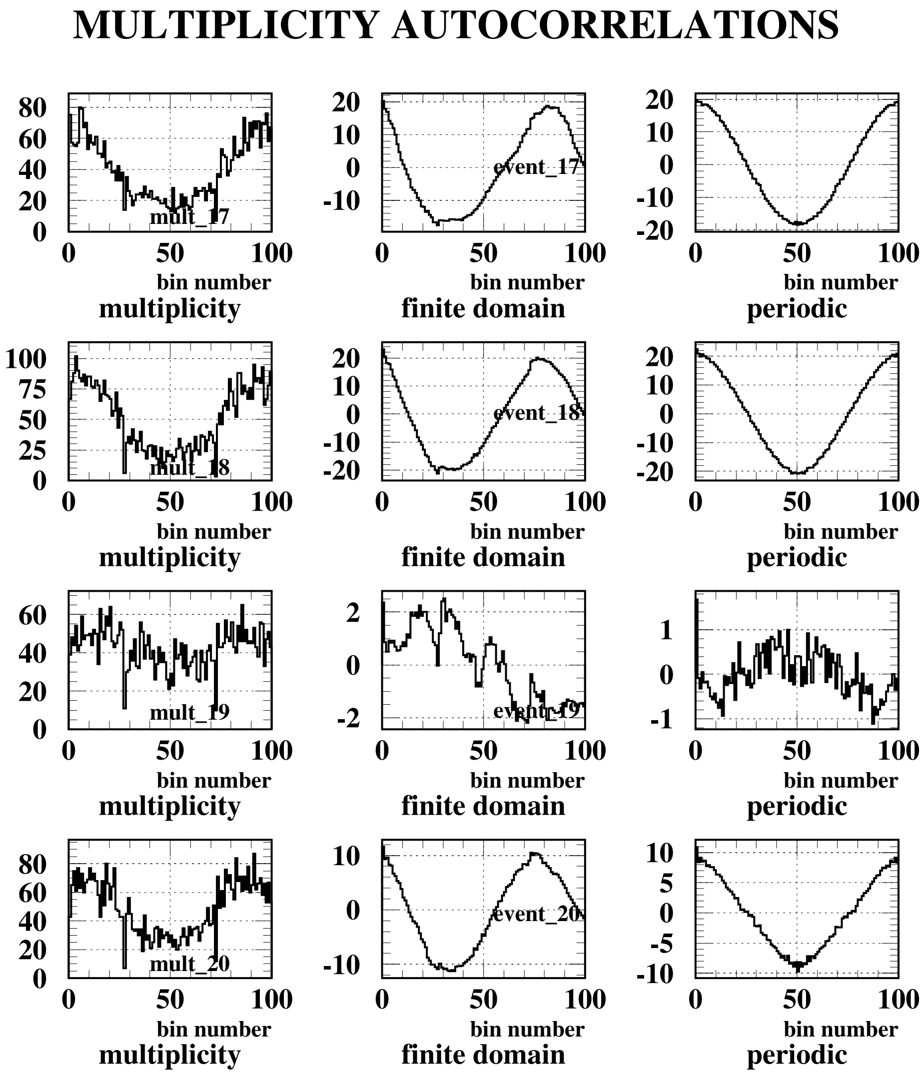
MULTIPLICITY AUTOCORRELATIONS
mult_17
event_17
bin number
multiplicity
finite domain
periodic
mult_18
event_18
mult_19
event_19
mult_20
event_20

Figure 17:

# 6 Statistical Error

It is useful to have a feeling for the level of random fluctuations in the differential autocorrelations. This can be determined by the following argument. The autocorrelation can be seen as a mean value of a hit density on some subset of a 2-D manifold. The manifold is $N \cdot N$ bins on which there are distributed $M^2$ hits. $M$ of these are special and fall on the diagonal of this space. These I disregard in the argument. They do not contribute to random error in the autocorrelation, but do indicate the level of random error in the primary distribution $f$ of hits on $N$ bins. For a Poisson distribution this leaves $M(M-1)$ hits distributed randomly on the 2-D manifold. The number of hits per bin follows a binomial distribution with $M(M-1)$ trials and a hit probability per trial of $1/N^2$. The variance of the distribution is therefore

$$\sigma_{bin}^2 = M(M-1) \cdot \frac{1}{N^2} \cdot (1 - \frac{1}{N^2}). \tag{12}$$

I will omit the last factor in subsequent expressions as being essentially unity.

The finite domain autocorrelation $B_m$ is essentially the mean value of the hit number in $N-m$ bins. Therefore the variance of this quantity is

$$\sigma_{B_m}^2 = \frac{1}{N-m} \cdot \frac{M(M-1)}{N^2}. \tag{13}$$

After normalization this becomes

$$\sigma_{B'_m}^2 = \frac{1}{N-m} \cdot \frac{N^2}{M(M-1)} \tag{14}$$

and the corresponding quantity for the differential autocorrelation is

$$\sigma_{b'_m}^2 = \frac{N-m}{M(M-1)}, \tag{15}$$

with corresponding variance

$$\sigma_{a'_m}^2 = \frac{N}{M(M-1)} \tag{16}$$

for the periodic autocorrelation form.

As an example, for $M$=4000 and $N$=100 the rms error in $a'_m$ is 0.25%. The rms error in the $b'_m$ is this value times the factor $\sqrt{\frac{M-m}{N}}$. Close inspection of the autocorrelation plots will illustrate both the correctness of this value and the $m$ dependence of the rms error $\sigma_{b'_m}$.

# 7 Power Spectra

These plots simply show the FT sine and cosine components for the FD autocorrelations for the twenty events. I don't consider further the periodic autocorrelation form because it contains less information. I show only the first twenty bins of the FT. In principle there are 50 independent bins (Nyquist criterion) for a 100 bin autocorrelation with real elements such as is the case here. However, only the first ten to fifteen bins of the FT have statistically significant contents for these generator events, indicating the 'long-wavelength' nature of the anomalous multiplicity contributions compared to the total domain of definition.

$$bs_k = \frac{2}{N}\sum_{m=1}^{N} b'_m \cdot sin(\frac{2\pi}{N}k \cdot m) \tag{17}$$

$$bc_k = \frac{2}{N}\sum_{m=1}^{N} b'_m \cdot cos(\frac{2\pi}{N}k \cdot m) \tag{18}$$

The chosen normalization means that these Fourier amplitudes are in 'units' of percent deviation corresponding to the differential autocorrelation. Thus, if no null hypothesis has been included in the definition of the $b_m$ then the required coefficients can be read directly off these plots in appropriate units. The quantities $bs_k$ and $bc_k$ are plotted in the following graphs as 'sine' and 'cosine.'

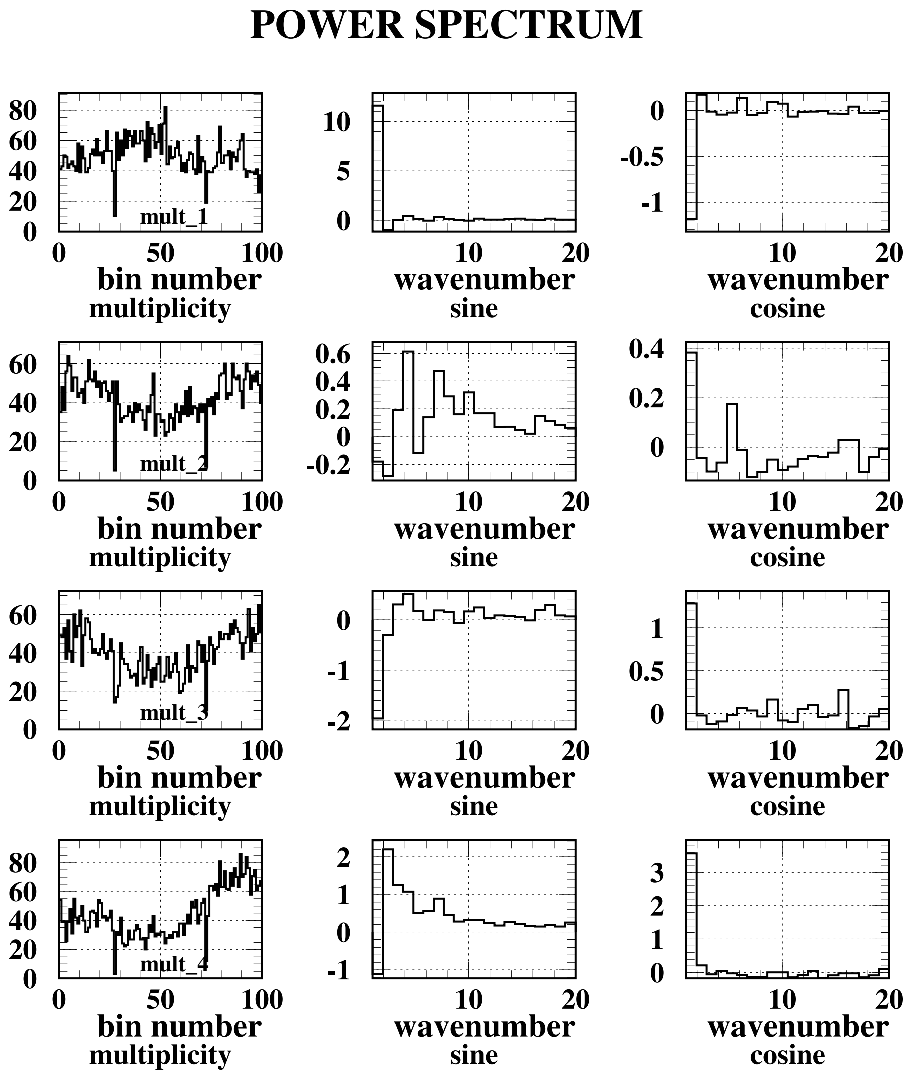
POWER SPECTRUM
mult_1
bin number
multiplicity
wavenumber
sine
wavenumber
cosine
mult_2
bin number
multiplicity
wavenumber
sine
wavenumber
cosine
mult_3
bin number
multiplicity
wavenumber
sine
wavenumber
cosine
mult_4
bin number
multiplicity
wavenumber
sine
wavenumber
cosine

Figure 18:

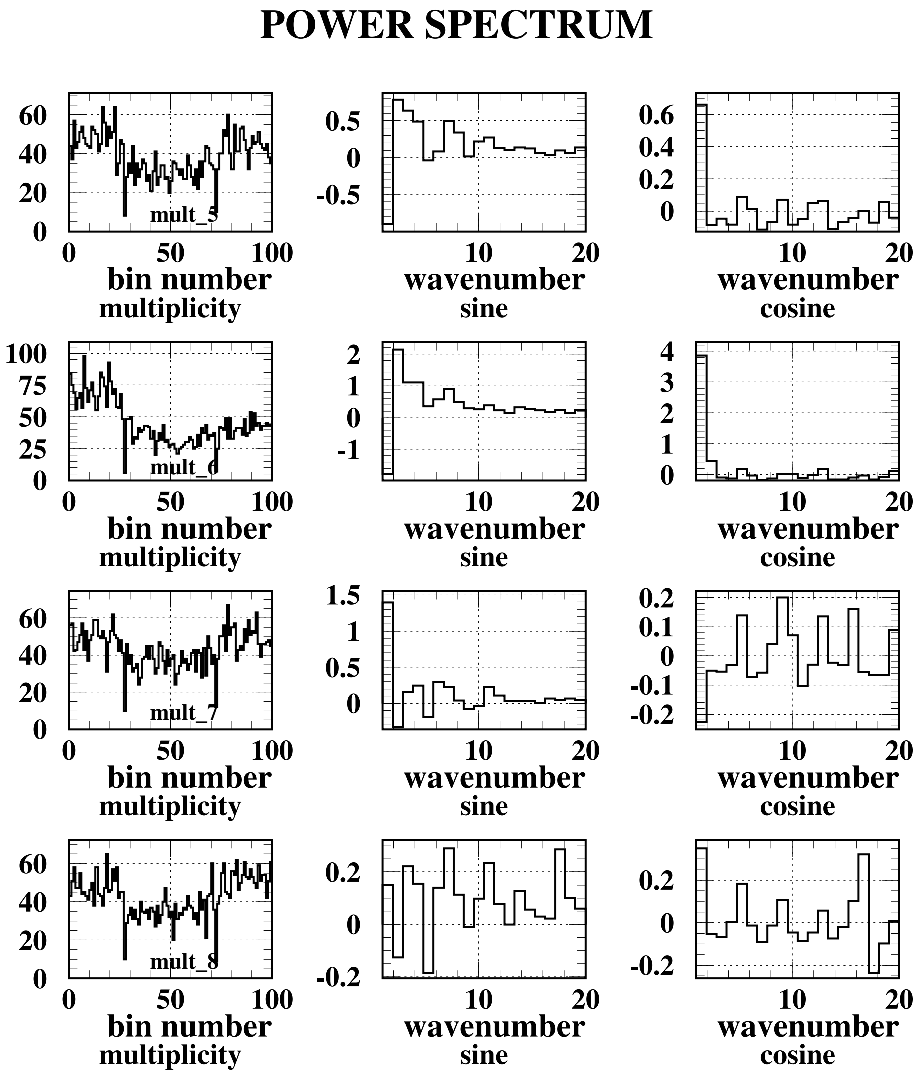
POWER SPECTRUM
mult_5
mult_6
mult_7
mult_8
bin number
multiplicity
wavenumber
sine
cosine

Figure 19:

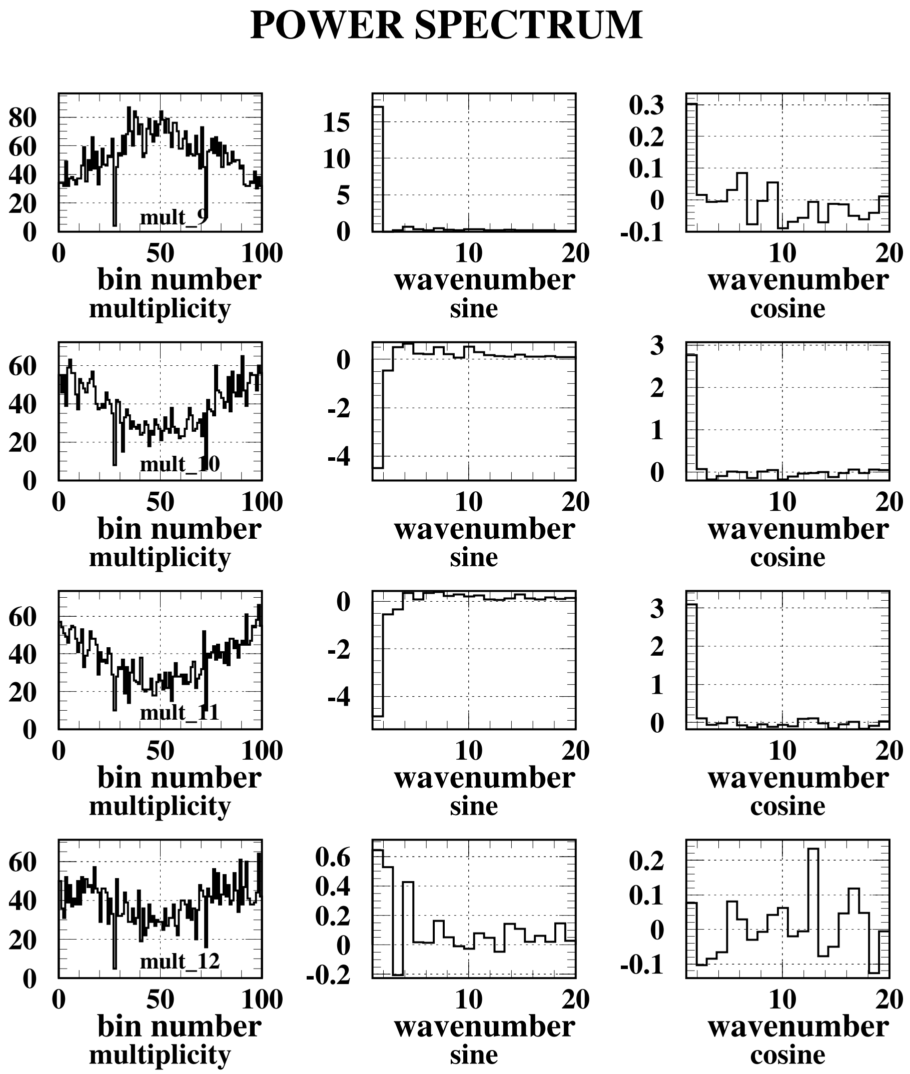
POWER SPECTRUM
mult_9
mult_10
mult_11
mult_12
bin number
multiplicity
wavenumber
sine
wavenumber
cosine

Figure 20:

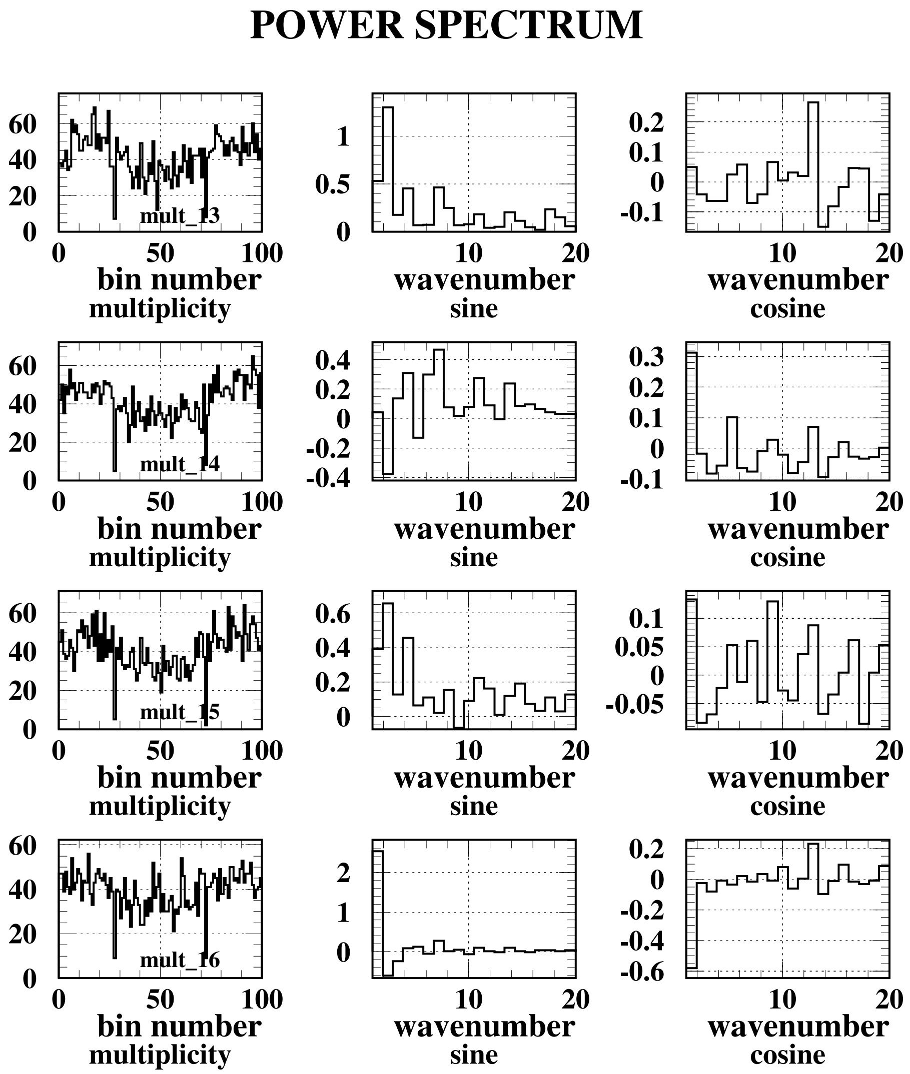
POWER SPECTRUM
mult_13
mult_14
mult_15
mult_16
bin number
multiplicity
wavenumber
sine
wavenumber
cosine

Figure 21:

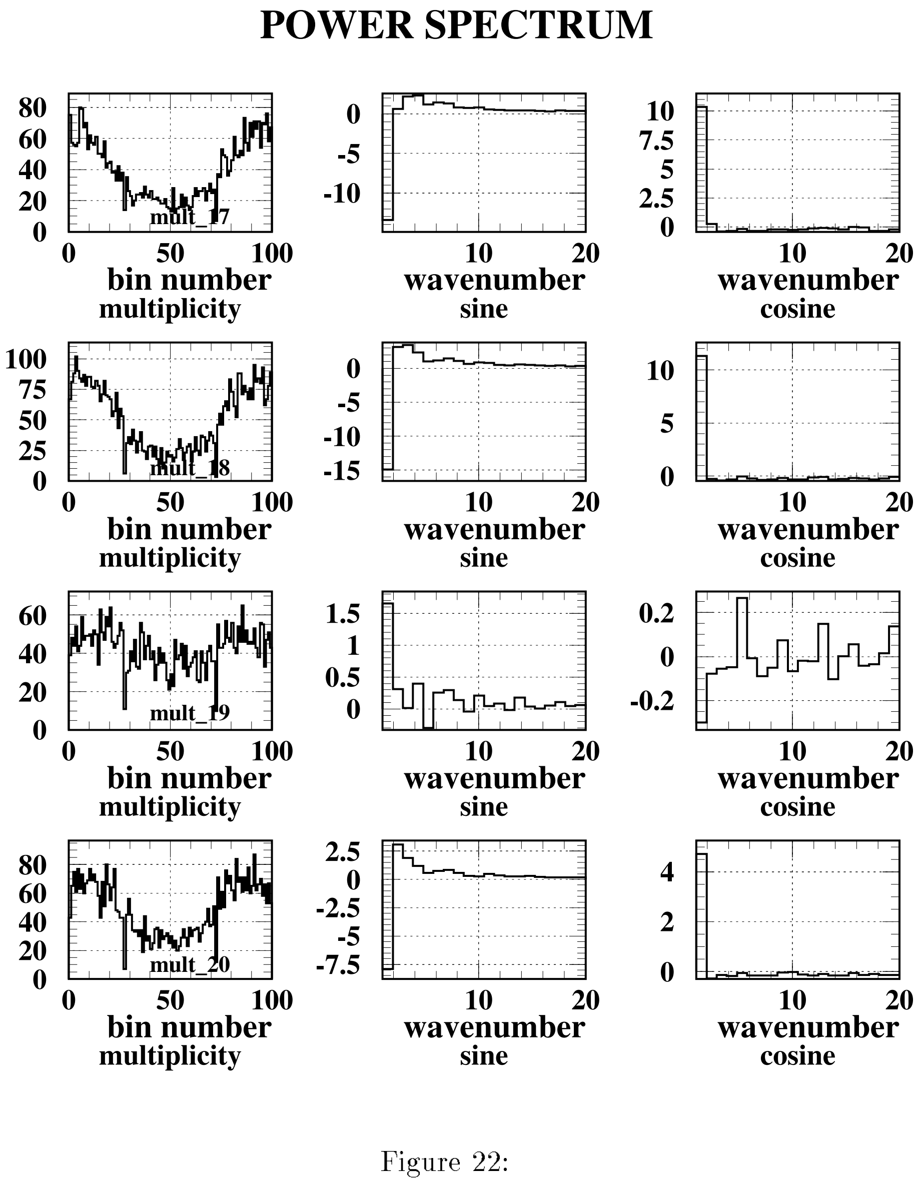
POWER SPECTRUM
mult_17
mult_18
mult_19
mult_20
bin number
multiplicity
wavenumber
sine
wavenumber
cosine

Figure 22:

## 8 Power/Phase Densities

In these figures I show the power density distributions and 'power-density weighted' phase distributions for the twenty events. The power density is defined as

$$P_k = bs_k^2 + bc_k^2 \tag{19}$$

with the 'total power'

$$P_0 \equiv \sum_{k=1}^{N/2} P_k. \tag{20}$$

The weighted phase density is defined as

$$\phi_k = tan^{-1}(bs_k/bc_k)P_k/P_0 \tag{21}$$

with the 'total phase' defined as

$$\phi_{tot} = \sum_{k=1}^{N/2} \phi_k. \tag{22}$$

I also define a second moment of the power density as

$$P_2 = \sum_{k=1}^{N/2} k^2 P_k/P_0 \tag{23}$$

The phase density definition is intended to include only statistically significant phase information.

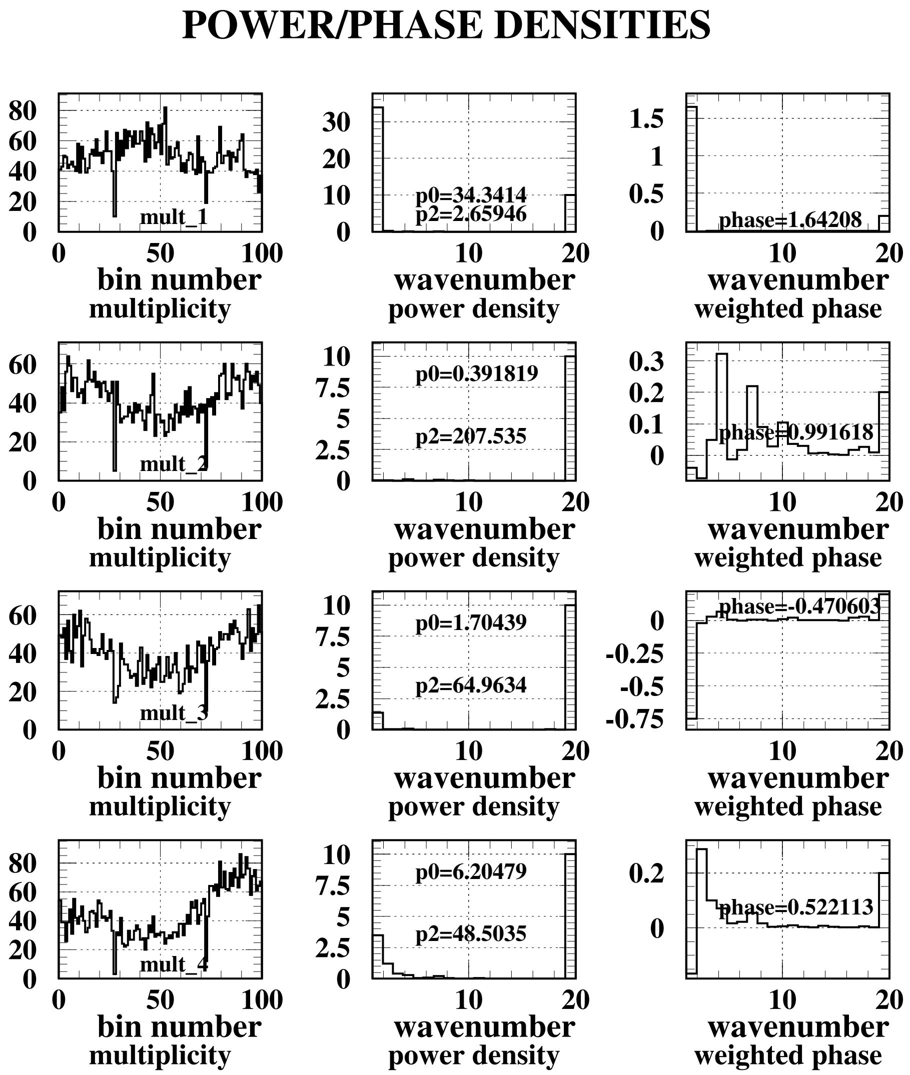
POWER/PHASE DENSITIES
mult_1
p0=34.3414
p2=2.65946
phase=1.64208
mult_2
p0=0.391819
p2=207.535
phase=0.991618
mult_3
p0=1.70439
p2=64.9634
phase=-0.470603
mult_4
p0=6.20479
p2=48.5035
phase=0.522113
bin number
multiplicity
wavenumber
power density
wavenumber
weighted phase

Figure 23:

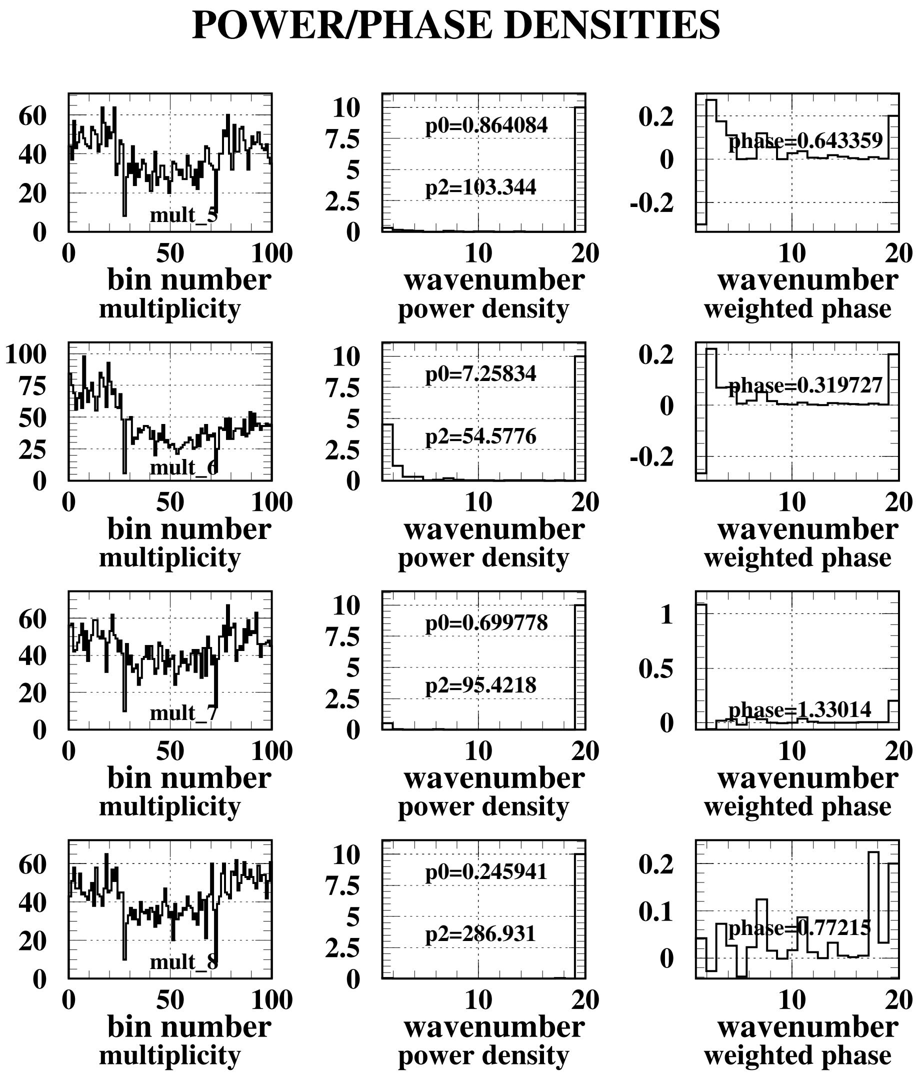
POWER/PHASE DENSITIES
mult_5
p0=0.864084
p2=103.344
phase=0.643359
mult_6
p0=7.25834
p2=54.5776
phase=0.319727
mult_7
p0=0.699778
p2=95.4218
phase=1.33014
mult_8
p0=0.245941
p2=286.931
phase=0.77215
bin number
multiplicity
wavenumber
power density
wavenumber
weighted phase

Figure 24:

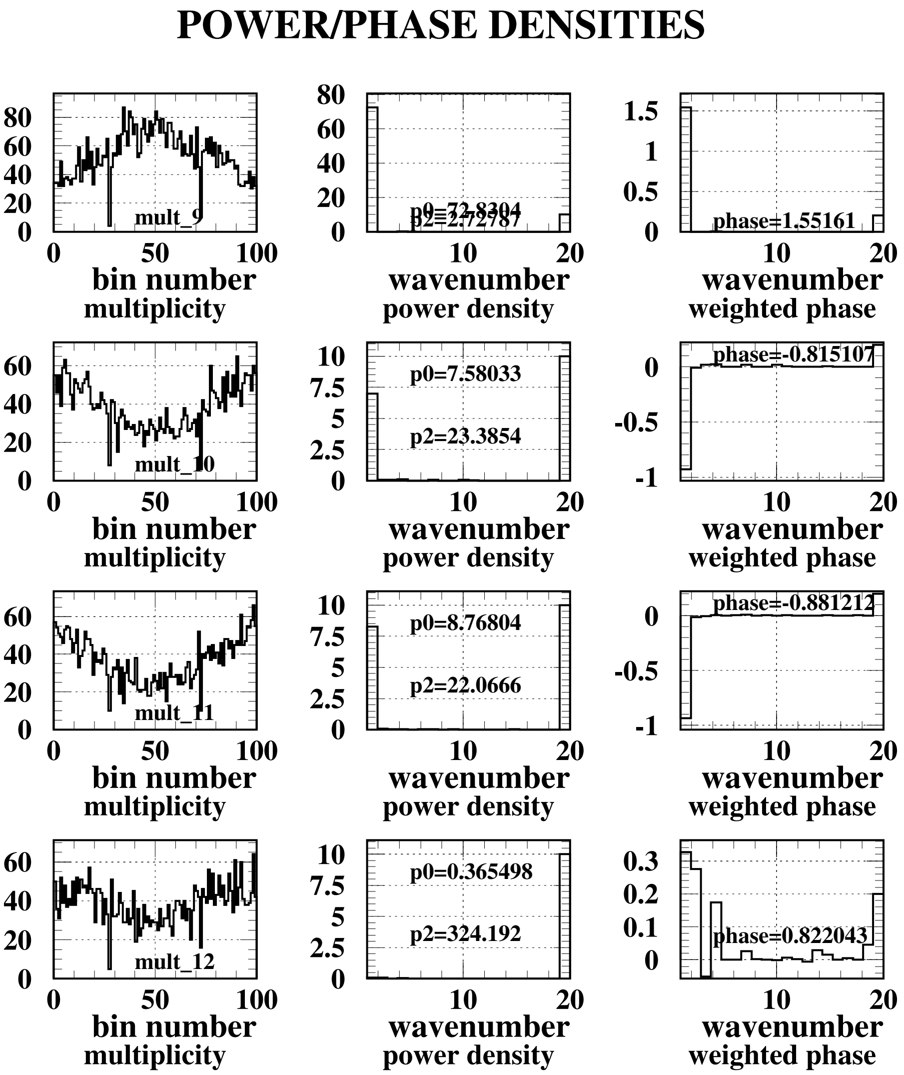

POWER/PHASE DENSITIES
mult_9
p0=72.8304
p2=2.72787
phase=1.55161
mult_10
p0=7.58033
p2=23.3854
phase=-0.815107
mult_11
p0=8.76804
p2=22.0666
phase=-0.881212
mult_12
p0=0.365498
p2=324.192
phase=0.822043
bin number
multiplicity
wavenumber
power density
wavenumber
weighted phase


Figure 25:

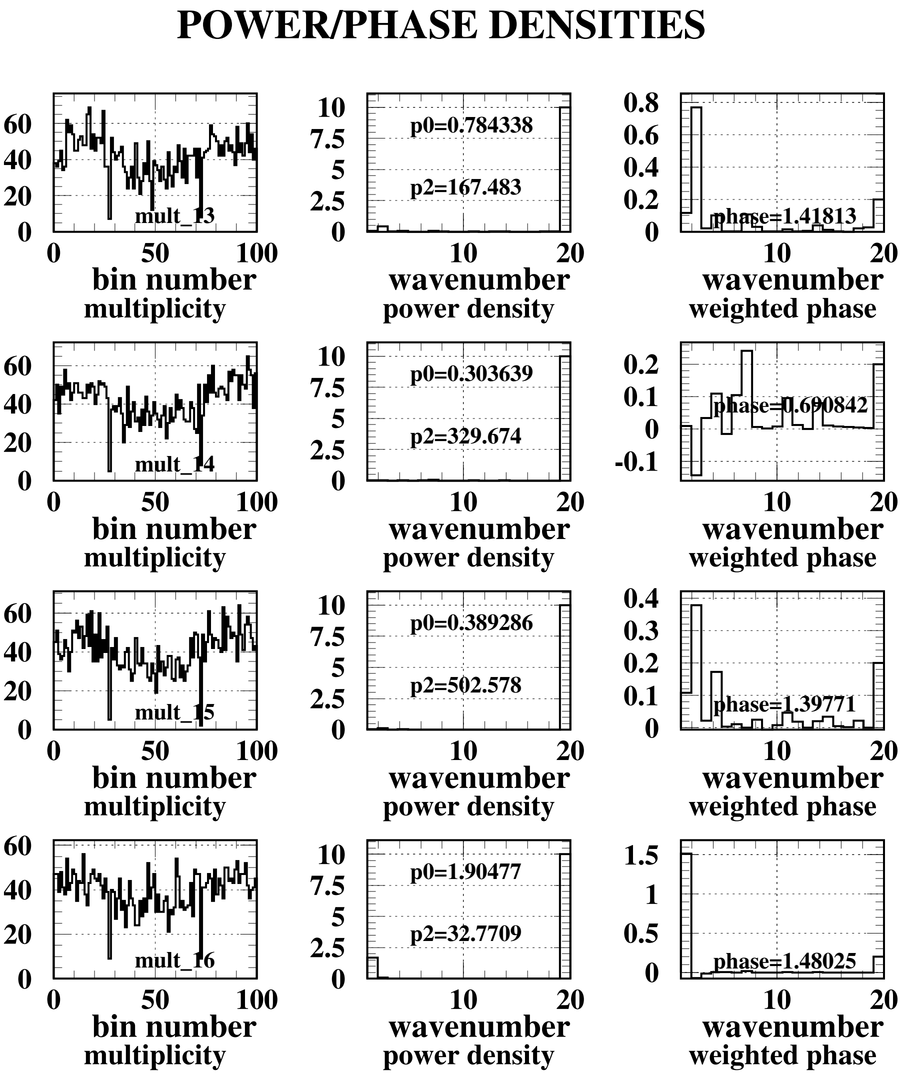
POWER/PHASE DENSITIES
mult_13
bin number
multiplicity
p0=0.784338
p2=167.483
wavenumber
power density
phase=1.41813
wavenumber
weighted phase
mult_14
bin number
multiplicity
p0=0.303639
p2=329.674
wavenumber
power density
phase=0.690842
wavenumber
weighted phase
mult_15
bin number
multiplicity
p0=0.389286
p2=502.578
wavenumber
power density
phase=1.39771
wavenumber
weighted phase
mult_16
bin number
multiplicity
p0=1.90477
p2=32.7709
wavenumber
power density
phase=1.48025
wavenumber
weighted phase

Figure 26:

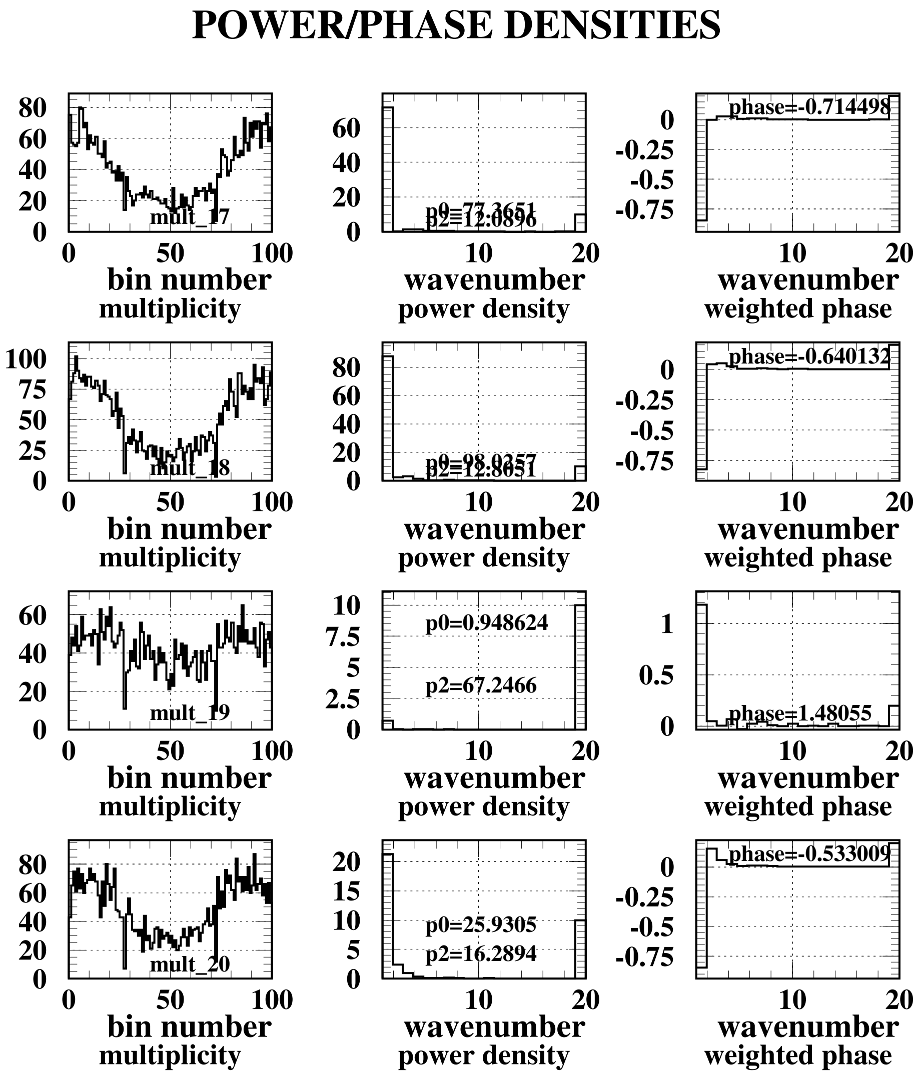
POWER/PHASE DENSITIES
mult_17
bin number
multiplicity
p0=77.3651
p2=12.0896
wavenumber
power density
phase=-0.714498
wavenumber
weighted phase
mult_18
bin number
multiplicity
p0=98.0257
p2=12.8651
wavenumber
power density
phase=-0.640132
wavenumber
weighted phase
mult_19
bin number
multiplicity
p0=0.948624
p2=67.2466
wavenumber
power density
phase=1.48055
wavenumber
weighted phase
mult_20
bin number
multiplicity
p0=25.9305
p2=16.2894
wavenumber
power density
phase=-0.533009
wavenumber
weighted phase

Figure 27:

# 9 Pattern Spaces

In Figs. 28 – 30 I present plots of total power *vs* total phase for each of the twenty generator events using two slightly different choices of null hypothesis. I also include in the third plot 100 'events' in each of which 4000 Poisson-distributed hits were scattered on the same domain of definition. In the analysis of these Poisson events all steps remained the same except that the null hypothesis components of the differential autocorrelations were omitted.

As one might hope, most of the events with anomalous contributions appear here with elevated total power ($P_0$) values. In addition, one can see that the defined 'total phase' provides very useful discrimination among these special events as regards the details of their formation. One can compare the distribution of these events on the defined power/phase pattern space with their locations on the $E_{tot} - Q_2$ space described above. The agreement between the two figures is surprisingly good.

In Fig. 28 the null hypothesis was that one which minized the total power for the ensemble of normal events. This choice resulted in this clearly isolated group moving to a large positive phase as well as minimum power. This tendency to positive phase for normal events is related to the details of the FD autocorrelation definition and the presence of the gaps in $\eta$ coverage.

In Fig. 29 I have altered one of the coefficients in the null hypothesis somewhat [$bs_1 : -7.5 \rightarrow -8.5$] to isolate as much as possible the normal events from the special events without concern for minimizing the power. The phase parameter is important here to provide very sharp isolation of the normal events.

In Fig. 30 I have altered two coefficients in the null hypothesis [$bs_1 : -7.5 \rightarrow -6$ and $bc_1 : 1.5 \rightarrow 0$] to bring the normal events near the zero phase line. This reduces the degree of selectivity in terms of the increased proximity of event 3 to the normal events for this choice.

Event 3, and to a lesser extent events 10 and 11 produce reduced power in this analysis in comparison to the other special events because of the limited $\eta$ acceptance of the trigger detector system [-2,2] in comparison to the $\eta$ range of the particle yield [-5,5]. This means that as the $Q_2$ of an event becomes large and negative (peaks further separated) the anomalous yield falls further outside the detector acceptance and so contributes less to the power in the differential autocorrelation. This is one incentive for making the trigger detector acceptance as large as possible in $\eta$.

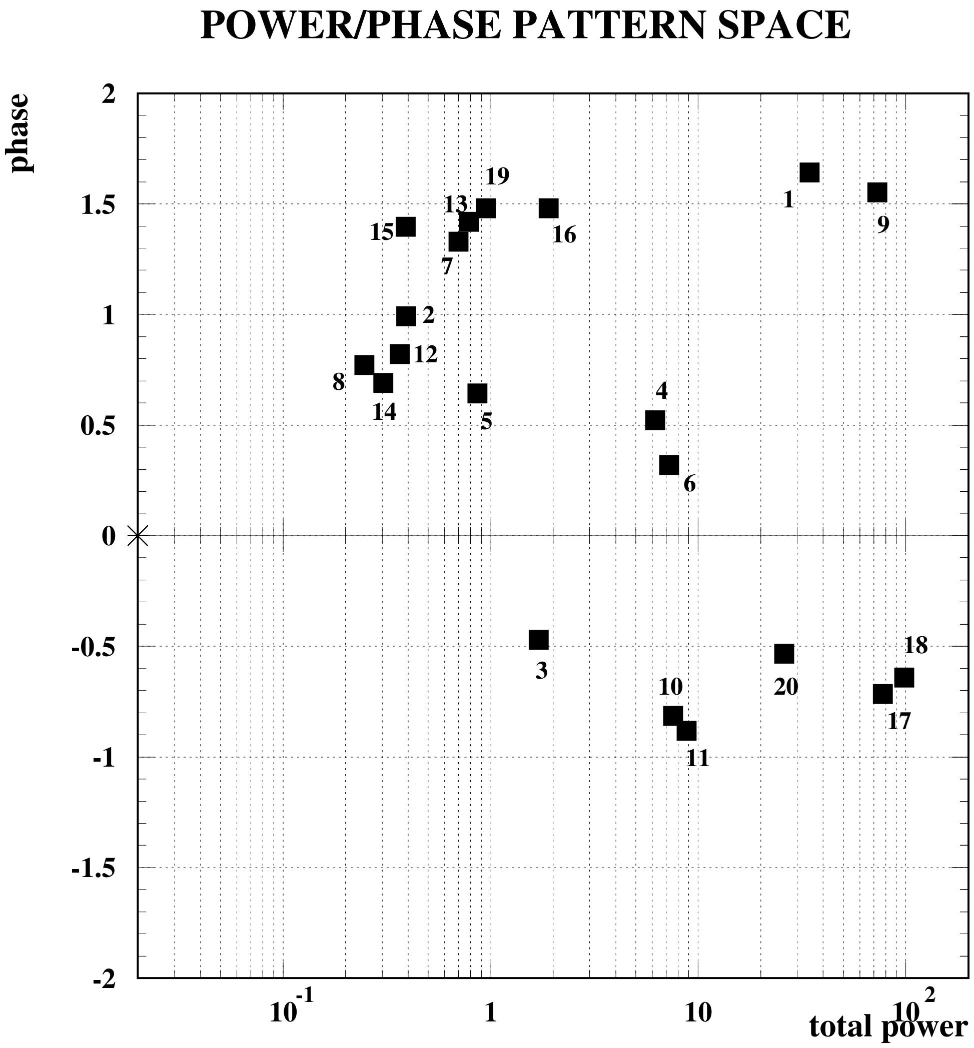
POWER/PHASE PATTERN SPACE
phase
total power
2
1.5
1
0.5
0
-0.5
-1
-1.5
-2
10^-1
1
10
10^2
1
2
3
4
5
6
7
8
9
10
11
12
13
14
15
16
17
18
19
20

Figure 28:

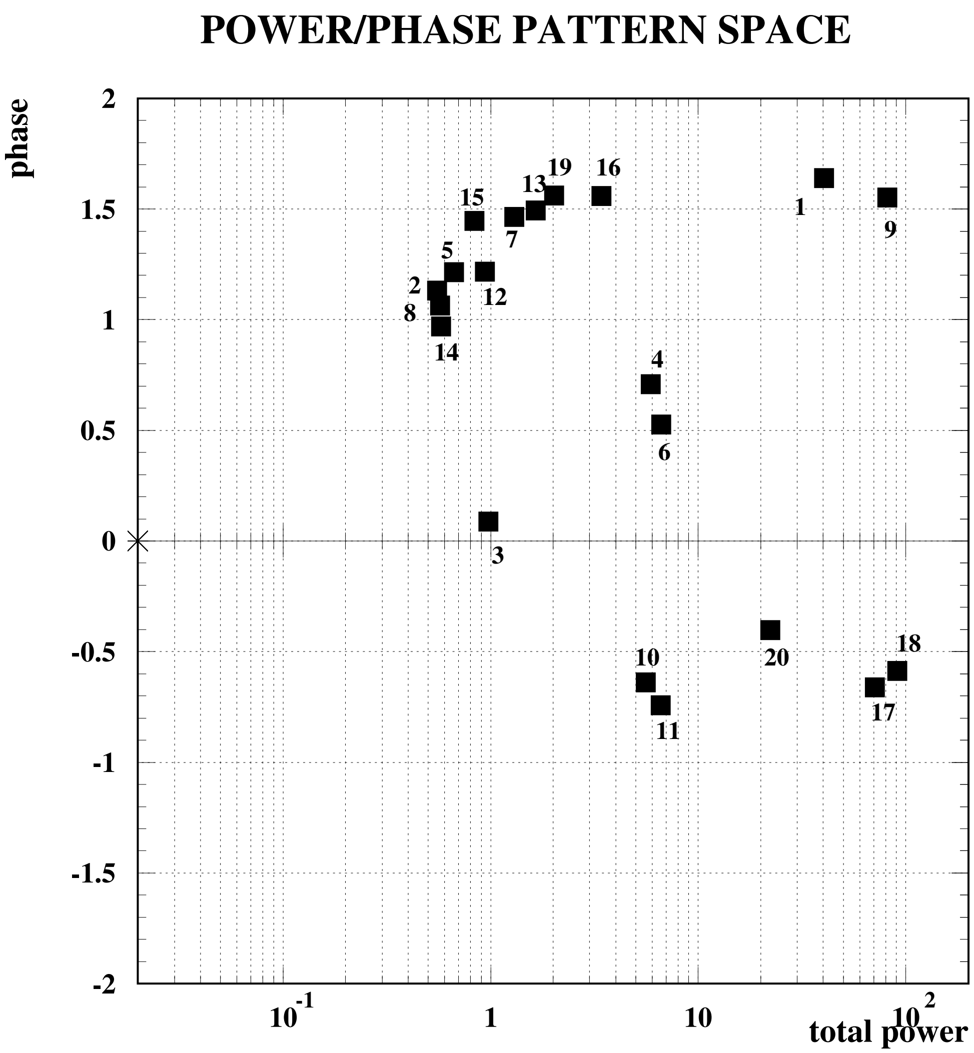
POWER/PHASE PATTERN SPACE
phase
2
1.5
1
0.5
0
-0.5
-1
-1.5
-2
10^-1
1
10
10^2
total power
1
2
3
4
5
6
7
8
9
10
11
12
13
14
15
16
17
18
19
20

Figure 29:

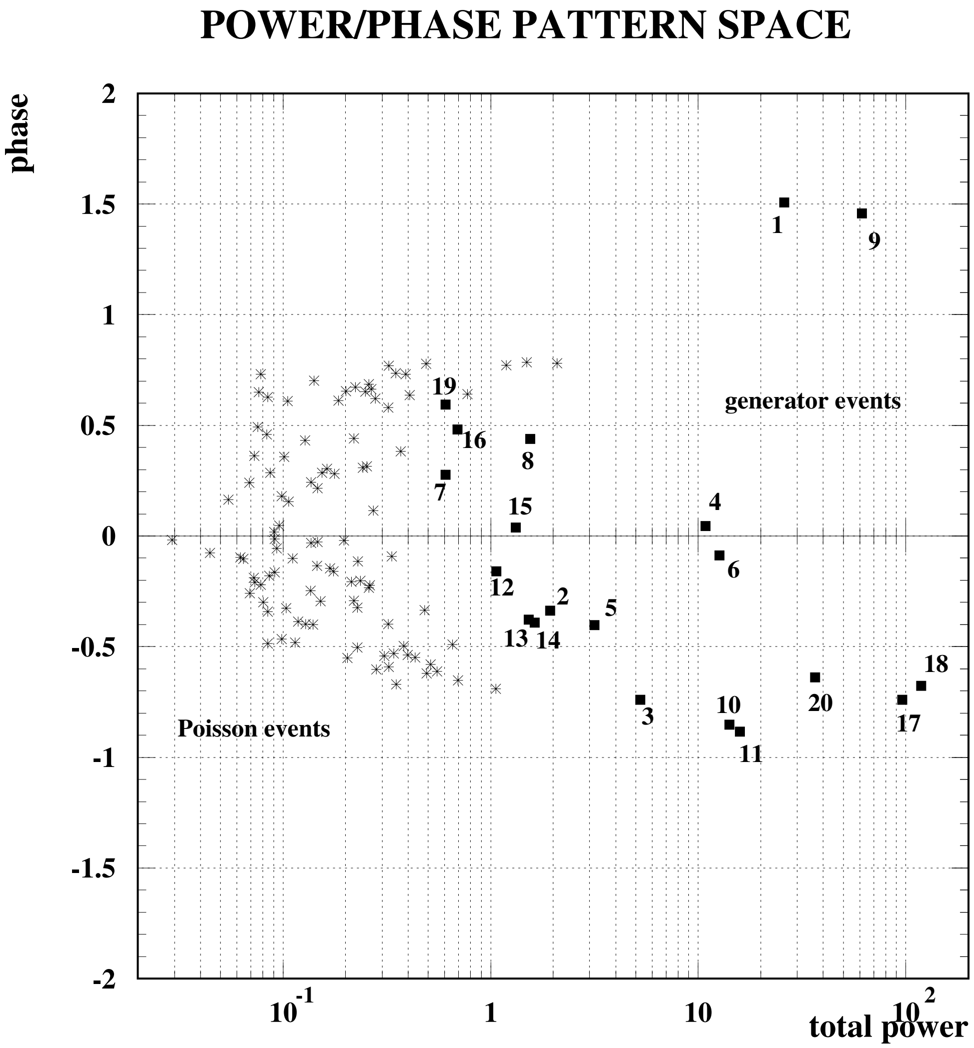
POWER/PHASE PATTERN SPACE
phase
2
1.5
1
0.5
0
-0.5
-1
-1.5
-2
$10^{-1}$
1
10
$10^{2}$
total power
generator events
Poisson events
1
9
19
16
8
7
15
4
6
12
2
5
13
14
3
10
11
20
18
17

Figure 30:

## 10 Summary

I have presented here the results of a power spectrum analysis of modified and unmodified HIJET events. I have collected the resulting plots together to give an idea of the details of the analysis chain based on autocorrelations and power spectra when applied to generator events processed through GEANT. The quantities used here to define a pattern space are not exhaustive, and different pattern spaces or higher-dimensional spaces may be preferable. The details of the space are not as important as the degree of independence of the various defined quantities. As in the design of a polygraph one wants a number of independent degrees of freedom defining a space which can be explored by simulations or by reactions to known inputs (truths and falsehoods or known anomalies). Once the space is defined in this manner it can be used to select events in a relatively bias-free way.

I thank Zoran Milosevich and Ron Longacre for providing the simulation data and helpful comments and corrections.